https://doi.org/10.5194/egusphere-2026-5104
Preprint. Discussion started: 23 September 2026

Modification of the Quasi-Biennial Oscillation by Stratospheric Water Vapor From the Hunga Tonga–Hunga Ha'apai Eruption

Jinpeng Lu[1,2,3,4], Sijia Lou[1,2,3*], Wuke Wang[5], Jiankai Zhang[6], Ke Ding[1,2,3], Xin Huang[1,2,3], Yiquan Jiang[1,7], Tengyu Liu[1,2,3], Yawen Liu[2,3], Qinyan Xie[8], Lian Xue[1,2,3], Zilin Wang[1,2,3], Chen zhou[1,2,3], Anbao Zhu[2,3], Aijun Ding[1,2,3]

[1]State Key Laboratory of Severe Weather Meteorological Science and Technology, Nanjing University, Nanjing 210023, China
[2]Joint International Research Laboratory of Atmospheric and Earth System Sciences (JirLATEST), Nanjing University, Nanjing 210023, China
[3]School of Atmospheric Sciences, Nanjing University, Nanjing 210023, China
[4]now at Chengdu Vocational & Technical College of Industry, Chengdu 610218, China
[5]Department of Atmospheric Science, China University of Geosciences, Wuhan 430074, China
[6]College of Atmospheric Sciences, Lanzhou University, Lanzhou 730000, China
[7]China Meteorological Administration Key Laboratory for Climate Prediction Studies, Nanjing University, Nanjing 210023, China
[8]Chengdu Research Institute of Education Science, Chengdu 610036, China

Correspondence to: S. Lou (lousijia@nju.edu.cn)

Abstract. The Hunga Tonga–Hunga Ha'apai (HTHH) undersea volcano injected approximately 0.5 Tg of sulfur dioxide (SO_2) and about 150 Tg of water vapor (H_2O) into the stratosphere. Using a combination of observations and model simulations, we investigate the response of the Quasi-Biennial Oscillation (QBO) to these stratospheric SO_2 and H_2O perturbations, as well as the dynamic mechanisms underlying the QBO modification. A portion of the sulfate aerosols and H_2O remained in the tropical stratosphere for over a year. The water-rich HTHH eruption significantly influenced the QBO amplitude, with the simulated 30 hPa QBO index anomalies accounting for 11–32% of the anomalies observed in the 2022 reanalysis data. The combined effect of H_2O and sulfate aerosols on stratospheric temperature is mainly concentrated in the tropical stratosphere (south of 15°N). H_2O-induced radiative cooling reshapes the residual circulation and tropical upwelling response, reducing the upward advective tendency acting on positive zonal wind perturbations in key regions and favoring their downward propagation into the 30–100 hPa layer. This process effectively modulates the amplitude of the stratospheric QBO through the “upwelling mechanism”. Additionally, the cooling of the stratosphere caused by H_2O and sulfate aerosols generates easterly and westerly wind shear through the “thermal wind balance mechanism” between April and October, further influencing the stratospheric QBO.

https://doi.org/10.5194/egusphere-2026-5104
Preprint. Discussion started: 23 September 2026

1 Introduction

Volcanic eruptions have widespread impacts on human economics, the environment, and the climate (Stone et al., 2017; Wang et al., 2023). Explosive volcanic eruptions can inject large amounts of sulfur dioxide (SO_2) into the upper troposphere and, in some cases into the stratosphere (Quaglia et al., 2023), along with volcanic ash and other gases (Babu et al., 2022; Brown et al., 2023). After being injected into the stratosphere, SO_2 is oxidized into sulfate aerosols (Santer et al., 2015; Toohey and Sigl, 2017; Bluth et al., 1992; Stone et al., 2018). These sulfate aerosols have a relatively long lifetime (~1-3 years) in the stratosphere (Wang et al., 2022; Gao et al., 2023) and can be transported globally by the Brewer-Dobson circulation (BDC), leading to their widespread distribution (Kremser et al., 2016; Tilmes et al., 2017). Once distributed in the stratosphere, sulfate aerosols play an important role in the Earth's radiative balance by scattering incoming solar radiation and thereby cooling the surface (Wang et al., 2023; Zhou et al., 2023), while also absorbing terrestrial longwave and near-infrared radiation (Kremser et al., 2016). This combination of radiative effects results in net heating in the lower tropical stratosphere (Timmreck, 2012; Zuo et al., 2018; Toohey et al., 2011), which perturbs the thermal structure of the tropical stratosphere and influences large-scale atmospheric dynamics (Bittner et al., 2016), including modulation of the quasi-biennial oscillation (QBO) (Aquila et al., 2014; Franke et al., 2021; Brown et al., 2023; Niemeier et al., 2020; Richter et al., 2017; Tilmes et al., 2017).

The QBO is a periodic oscillation with an approximate period of 28 months, characterized by alternating tropical zonal easterly and westerly winds in the stratosphere, typically between 16 and 40 km altitude (Brown et al., 2023; Aquila et al., 2014; Baldwin et al., 2001). This oscillation is driven by vertically propagating equatorial waves, including Kelvin and Rossby-gravity waves, which deposit momentum into the mean flow and generate the alternating wind regimes (Baldwin et al., 2001; Franke and Giorgetta, 2024). These wind regimes propagate downward from the upper stratosphere (above 5 hPa) towards the tropopause (Brown et al., 2023). The rate of downward propagation is determined by the balance between wave-driven acceleration and the vertical advection of momentum by troptical upwelling associated with BDC (Baldwin et al., 2001; Aquila et al., 2014; Brown et al., 2023). Previous studies have shown that the QBO exerts a significant influence on a wide range of atmospheric processes (Anstey et al., 2021; Wang et al., 2025; Trepte and Hitchman, 1992; Garfinkel and Hartmann, 2011). For example, on shorter timescales, the QBO modulates tropical convection, circulation, and weather systems (Son et al., 2017), while on seasonal to interannual timescales it is closely linked to stratospheric sudden warming events and variations in the strength of the polar vortex (Anstey et al., 2021; Wang et al., 2025). Consequently, the QBO plays an important role in both weather and climate (Scaife et al., 2014).

Following volcanic eruptions, radiative heating induced by stratospheric sulfate aerosols in the lower stratosphere enhances tropical upwelling and modifies the downward propagation of QBO shear zones (Aquila et al., 2014). For example, sulfate aerosols formed after the 1991 Mount Pinatubo eruption led to a warming of approximately 3.5 K in the lower stratosphere, delaying the downward propagation of easterly shear and resulting in a prolonged persistence of westerly shear in the lower stratosphere (Labitzke, 1994). Model studies further report that sustained SO_2 injection can lengthen the QBO period and

https://doi.org/10.5194/egusphere-2026-5104
Preprint. Discussion started: 23 September 2026

favor persistent westerly shear regimes (Aquila et al., 2014; Richter et al., 2017; Franke et al., 2021; Brown et al., 2023; Ferraro et al., 2012).

The modulation of the QBO by volcanic aerosols is primarily explained by two mechanisms: the "upwelling mechanism" and the "thermal wind balance mechanism" (Aquila et al., 2014; Franke et al., 2021). The upwelling mechanism is associated with aerosol-induced radiative heating in the tropical lower stratosphere, which strengthens the upward branch of the BDC. The resulting enhancement of tropical upwelling increases the vertical advection of momentum, thereby reducing the descent rate of QBO shear zones and influencing their downward progression and amplitude (Bittner et al., 2016; Franke et al., 2021). Under typical sulfate-driven warming, this effect tends to delay the descent of easterly shear and favor persistent westerly shear in the tropical lower to middle stratosphere (DallaSanta et al., 2021; Brown et al., 2023). In addition, sulfate-induced rediative heating modifies the meridional temperature structure in the lower stratosphere, altering temperature gradients between the tropics and subtropics. Through thermal wind balance, these changes induce zonal wind shear and therby modifying the vertical structure of the QBO.

These two mechanisms are not independent and can operate simultaneously. Their combined effects lead to a QBO response that depends on both the background QBO phase and the magnitude of volcanic forcing (Brown et al., 2023). Following the Pinatubo eruption, the period and amplitude of the QBO were strongly influenced by the phase at the time of the eruption: eruption occurring during the westerly phase tend to extend the QBO period, whereas those during the easterly phase tend to shorten it (Dallasanta et al., 2021). Previous studies indicated that, for typical sulfate-dominated volcanic eruptions, the upwelling mechanism plays a dominant role in modulating the QBO by directly affecting the downward propagation of shear zones, particularly in the early stage of the perturbation. In contrast, the thermal wind balance mechanism is generally weaker initially but may become more important over longer timescales by modifying the meridional structure of the zonal wind (Aquila et al., 2014; Brown et al., 2023). Under stronger forcing conditions (e.g., SO_2 emissions approximately 60 times that of the Pinatubo eruption), however, the QBO response becomes less dependent on the initial phase and is more strongly influenced by thermal wind balance mechanism, which primarily modifies the zonal wind structure (Brenna et al., 2021).

Traditional volcanic eruptions primarily inject large amounts of SO_2 into the atmosphere, and previous studies have mainly focused on the chemical and climatic effects associated with the formation of sulfate aerosols. However, the eruption of Hunga Tonga–Hunga Ha'apai (HTHH) volcano (20.54°S,175.38°W) on 15th January 2022 was significantly different (Proud et al., 2022). Unlike typical SO_2-rich eruption, the HTHH eruption injected an exceptionally large amount of water vapor (H_2O) into the stratosphere while releasing only a relatively small amount of SO_2. Satellite observations from the Microwave Limb Sounder (MLS) indicate that the eruption increased the stratospheric H_2O burden by around 150 Tg, corresponding to an increase of about 10% (Randel et al., 2023; Zhou et al., 2024). In contrast, the SO_2 injection was only about 0.5 Tg, nearly 30 times smaller than that of the Pinatubo eruption (Carn et al., 2022). Stratospheric H_2O is a greenhouse gas and a source of OH radical, and also contributes to the formation of polar stratospheric clouds (PSCs) (Solomon et al., 2015). H_2O from the HTHH eruption significantly altered the radiative balance, dynamics, and photochemistry of the stratosphere in the months

https://doi.org/10.5194/egusphere-2026-5104
Preprint. Discussion started: 23 September 2026

following the eruption (Xia et al., 2022; Xia et al., 2021), including net cooling of stratospheric temperatures (Schoeberl et al., 2022; Sellitto et al., 2022; Zhang et al., 2025). As a result of warming induced by sulfate aerosols and cooling induced by enhanced stratospheric H_2O, the HTHH eruption represents a fundamentally different radiative forcing compared with typical SO_2-rich volcanic eruptions, with potentially distinct impact on the QBO.

In this study, we investigate the effects of SO_2 and H_2O injections from HTHH eruptions on the stratospheric QBO. Section 2 describes the datasets, model simulations, and methods. Section 3 presents the QBO and temperature responses. Section 4 analyses the underlying dynamic mechanisms, and section 5 provides a discussion and conclusions.

2 Data, Models and Methods

2.1 Satellite observations

The Microwave Limb Sounder (MLS) instrument was launched on NASA's Aura satellite on 15 July 2004 into a sun-synchronous orbit with equator crossing times of 01:45 LST (descending orbits) and 13:45 LST (ascending orbits) (Ern et al., 2022). MLS utilizes five broad microwave spectral regions, with centers ranging approximately from 118 to 2500 GHz, in a limb-viewing configuration to measure various atmospheric microwave emissions in a limb-viewing geometry (Waters et al., 2006), from which temperature and numerous trace gas species are retrieved. For this work, we use MLS version 5.1 H_2O and SO_2 products. Spatial coverage is near-global (82°S–82°N) and the vertical resolution of the H_2O retrievals varies with pressure, from ~1.5 km at 316 hPa to about 3.5 km to 4.64 hPa, and degrades to ~15 km above 0.1 hPa, covering pressure levels 316 hPa to 0.00215 hPa. The vertical range of the SO_2 retrievals is from 215 to 10 hPa, with a vertical resolution of about 3 km. The anomalies for 2022 are calculated as deviations from the climatological mean over 2007–2021, and we focus on anomalies that exceed the range of previous variability.

The Suomi National Polar-orbiting Partnership (NPP) Ozone Monitor and Profiler Suite Limb Profiler (OMPS-LP) Level 3 aerosol extinction coefficient monthly gridded product provides stratospheric aerosol measurements derived from the OMPS-LP sensor onboard the Suomi-NPP satellite (Jaross et al., 2014). This Level 3 product provides spatially and temporally averaged data for selected retrieved quantities, including aerosol extinction coefficient, aerosol-to-molecular extinction ratio, number density, and aerosol optical depth. Each granule contains data from the daylight portion of each orbit averaged over an entire month in 5°×15°latitude–longitude grids. Spatial coverage is global (90°S–90°N). The profiles are gridded from the surface up to about 41 km with a vertical resolution of 1.0 km. We used the Aerosol Optical Depth at 510 nm (AOD_{510}) to characterize stratospheric aerosols.

2.2 ERA5 reanalysis dataset

The monthly zonal wind used in this study is derived from the fifth generation European Centre for Medium-Range Weather Forecasts atmospheric reanalysis of the global climate (ECMWF) reanalysis dataset, ERA5, with a horizontal resolution of 0.25°×0.25° for the period 2007–2022 (Hersbach et al., 2020). The dataset is provided on 137 model levels, extending from

https://doi.org/10.5194/egusphere-2026-5104
Preprint. Discussion started: 23 September 2026

the surface to approximately 0.01 hPa. For convenience, the data are interpolated to 37 pressure levels (0.1–1000 hPa), covering the troposphere, stratosphere, and part of the middle atmosphere (Hersbach et al., 2020). This vertical structure meets the needs of both tropospheric and stratospheric studies. The 30 hPa and 50 hPa QBO indices are defined as the zonal-mean zonal wind at the equator (2°S–2°N) at the corresponding pressure levels (Randel and Wu, 1996; Lu et al., 2019). Since 2022 corresponds to a transition from easterly to westerly QBO (EQBO to WQBO), the 30 hPa QBO index is classified as EQBO when it is less than -5 m/s and as WQBO when it is greater than 5 m/s (Lu et al., 2019; Mo and Hu, 2024). This threshold-based definition is used to distinguish QBO phases for subsequent analysis.

2.3 Model Simulations

2.3.1 Model Description

We used the Whole Atmosphere Community Climate Model version 6.0 (WACCM6) coupled with the global Community Earth System Model 2 (CESM2) (Bogenschutz et al., 2018; Gettelman et al., 2019) to simulate the QBO response due to the HTHH eruption. WACCM6 includes comprehensive chemistry spanning the Troposphere, Stratosphere, Mesosphere, and Lower Thermosphere (TSMLT), as well as interactive aerosol-cloud processes (Mills et al., 2016). The model is configured with 70 vertical layers extending up to about 140 km and a horizontal resolution of 0.95° × 1.25° (Tilmes et al., 2019; Liu et al., 2021). WACCM6 incorporates a comprehensive representation of physical and chemical processes relevant to stratospheric dynamics and aerosol evolution (Gettelman et al., 2019), enabling the simulation of radiative forcing and aerosol transport following volcanic eruptions. In particular, the model includes oxidation processes for sulfur-containing gases and H_2SO_4, allowing it to simulate volcanic SO_2 injections and their subsequent conversion into sulfate aerosols (Mills et al., 2016). In WACCM6, aerosols are represented using the Modal Aerosol Module version 4 (MAM4), which describes aerosol populations using a modal framework with four lognormal modes (Ge et al., 2021). This module simulates aerosol microphysical processes and lifecycle evolution, including nucleation, condensation, coagulation, aging, and removal processes such as dry and wet deposition. Major aerosol species represented in the model include sulfate, ammonium, black carbon, organic carbon, dust, and sea salt aerosols (Liu et al., 2016). With its relatively high vertical resolution and representation of wave-driven processes, including improved gravity wave parameterization (Guarino et al., 2024), WACCM6 can internally generate a QBO-like oscillation, that is consistent with observed characteristics (Fu et al., 2020), allowing it to reproduce the response of QBO shear-zone propagation, phase, and amplitude to volcanic perturbations (Gettelman et al., 2019; Brenna et al., 2021).

2.3.2 Model Design

In this study, four groups of experiments are conducted (Table 1). As a baseline simulation (base run), a no-volcanic-emissions experiment is performed, in which no volcanic SO_2 or H_2O emissions are included in either the troposphere or stratosphere. The model is integrated for 31 years, with the first 11 years discarded as spin-up, and the remaining 20 years

https://doi.org/10.5194/egusphere-2026-5104
Preprint. Discussion started: 23 September 2026

used for analysis. Based on ERA5 reanalysis data, the QBO transitioned from a westerly to an easterly phase in 2022, as indicated by zonal-mean winds averaged over 2°S–2°N at 10–100 hPa (Fig. S1a). To reproduce this real-world background state, one year from the final 20 years of the base run is selected that best matches the observed 2022 QBO phase in 2022 (denoted as sim_select; Fig. S1b). The QBO index at 30 hPa shows consistent variability between ERA5 and sim_select (Fig. S1c and d), indicating that the selected year provides a suitable initial condition for the sensitivity experiments starting in January. Based on this configuration, three sets of sensitivity ensemble experiments (sim_control, sim_SO_2 and sim_SO_2+H_2O) are performed (Table 1). Each experiment includes 20 ensemble members to isolate the forced response. The reported anomalies are defined as the difference between the ensemble mean of the forcing experiments and that of the control experiment.

In the volcanic forcing experiments, a total of 0.5 Tg of SO_2 is injected into the stratosphere at 20–30 km around 20.5°S. The injection is applied continuously during January with a constant emission rate in each simulation. H_2O is injected following the same approach, with a total emission of 145.8 Tg. After the SO_2 from the HTHH eruption fully entered the stratosphere, it is found that simulated SO_2 emissions in sim_SO_2+H_2O are consistent with the results of the MLS satellite data on 18 January 2022 (Fig. S2a and b). Furthermore, the simulated monthly H_2O anomalies from sim_SO_2+H_2O for January 2022 agree well with MLS data (Fig. S3), providing confidence in the representation of volcanic perturbations in the model.

Table 1. Simulation design.

Experiments	**Specified SO_2 and H_2O Forcing**	**Initial condition**
base run	no volcanic SO_2 or H_2O emissions in the troposphere or stratosphere	free run
sim_control	no volcanic SO_2 or H_2O emissions in the troposphere or stratosphere	sim_select
sim_SO_2	volcanic SO_2 injection in the stratosphere	sim_select
sim_SO_2+H_2O	both volcanic SO_2 and H_2O injection in the stratosphere	sim_select

2.4 Calculation of Brewer-Dobson circulation

The BDC is calculated in a pressure coordinate system (Edmon et al., 1980):

$$\overline{v}^* = \overline{v} - \left[\left(\overline{v'\theta'}\right)/\overline{\theta}_p\right]_p$$

$$\overline{\omega}^* = \overline{\omega} + (a\cos\varphi)^{-1}\left[\cos\varphi\left(\overline{v'\theta'}/\overline{\theta}_p\right)\right]_\varphi$$

where $\overline{v}$ is the mean meridional wind, θ is the potential temperature, $\overline{\omega}$ is average vertical velocity and a is the radius of the earth. The subscripts p and φ represent derivatives with pressure p and latitude φ, respectively. The overbar denotes the zonal mean and the prime denotes the deviations from the zonal mean value.

https://doi.org/10.5194/egusphere-2026-5104
Preprint. Discussion started: 23 September 2026

2.5 Calculation of Eliassen-Palm (EP) flux

The EP flux (Andrews et al., 1987) is calculated to diagnose wave activity propagation and wave-mean flow interaction in the stratosphere. The meridional (F_y) and vertical (F_z) components of the EP flux in spherical geometry are expressed as (Zhang et al., 2019; Lu et al., 2023):

$$F_y = \rho_0 a \cos\varphi \,(\overline{u}_z \overline{v'\theta'}/\overline{\theta}_z - \overline{u'v'})$$

$$F_z = \rho_0 a \cos\varphi \,\{[f - a(\cos\varphi)^{-1}(\overline{u}\cos\varphi)_\varphi]\overline{v'\theta'}/\overline{\theta}_z - \overline{w'v'}\}$$

And the divergence is expressed as:

$$\mathrm{div}\mathbf{F} = \nabla \cdot \mathbf{F}/(\rho_0 a \cos\varphi)$$

Here, ρ_0 is the air density, a is the radius of Earth, φ is the latitude, u and v represent the zonal and meridional winds, respectively, z is the altitude, θ is the potential temperature; f is the Coriolis parameter; and w is the vertical velocity. Overbars denote zonal means, and primes denote deviations from the zonal mean.

2.6 Calculation of Thermal Wind Balance

Thermal wind balance describes the dynamical relationship between the vertical shear of the zonal mean zonal wind ($\overline{U}_z$) and the zonal mean meridional temperature gradient ($\overline{T}_y$). It can be expressed as (Franke et al., 2021; Holton, 2004):

$$\overline{U}_z = -R(H\beta y)^{-1}\overline{T}_y$$

for an equatorial β plane. Assuming equatorial symmetry of the zonal mean temperature field, one can set $\overline{T}_y$=0 K km^{-1} at the Equator and apply the rule of L'Hospital:

$$\overline{U}_z = -R(H\beta)^{-1}\overline{T}_{yy}$$

R denotes the gas constant for dry air, H denotes the scale height, and β denotes the meridional gradient of the Coriolis parameter at the Equator. $\overline{T}_{yy}$ denotes the meridional curvature of the zonal mean temperature.

3 QBO response to tropical water-rich HTHH eruption

3.1 Stratospheric Sulfate Evolution

To analyze the impact of the water-rich HTHH eruption on stratospheric sulfate aerosols, we examine the monthly evolution of SO_2 and sulfate aerosol perturbations (defined as differences relative to the no-volcanic control simulation) in the sim_SO_2+H_2O and sim_SO_2 experiments for 2022 (Fig. 1a and b). In January, SO_2 and H_2O are injected into the tropical stratosphere at 5–100 hPa. Although the prescribed SO_2 emissions are identical in both experiments, SO_2 perturbations are

https://doi.org/10.5194/egusphere-2026-5104
Preprint. Discussion started: 23 September 2026

smaller in sim_SO_2+H_2O (Fig. 1a) than in sim_SO_2 (Fig. 1b) over 10°S–10°N at 10–100 hPa. In both experiments, SO_2 perturbations reach their maximum in February (Fig. 1a and b).

In the stratosphere, SO_2 is primarily oxidized by · OH radicals to form H_2SO_4, which subsequently contributes to sulfate aerosol formation (Kremser et al., 2016). Enhanced H_2O in sim_SO_2+H_2O increases · OH concentrations, thereby accelerating the conversion of SO_2 to sulfate aerosols. As a result, SO_2 perturbations are reduced, while sulfate perturbations are enhanced in sim_SO_2+H_2O compared to sim_SO_2 (Fig. 1a and b). The contrast becomes more evident when considering the difference between the two experiments (sim_SO_2+H_2O minus sim_SO_2; Fig. 1c and d). In the tropical stratosphere, the enhanced oxidation leads to an additional SO_2 decrease of about 0.08 ppbv in February (Fig. 1c), accompanied by an increase in sulfate aerosol concentrations of approximately 0.01 μg/m^3 (Fig. 1d). This pattern persists during the first few months following the eruption, indicating a more rapid sulfur conversion pathway in the presence of enhanced H_2O. Consequently, sulfate aerosol perturbations remain larger in sim_SO_2+H_2O throughout the year, particularly in the tropical stratosphere (Fig. 1d). and hence the SO_2 entering the stratosphere from the HTHH eruption can complete its conversion about one month earlier and thus have an impact on the stratosphere.

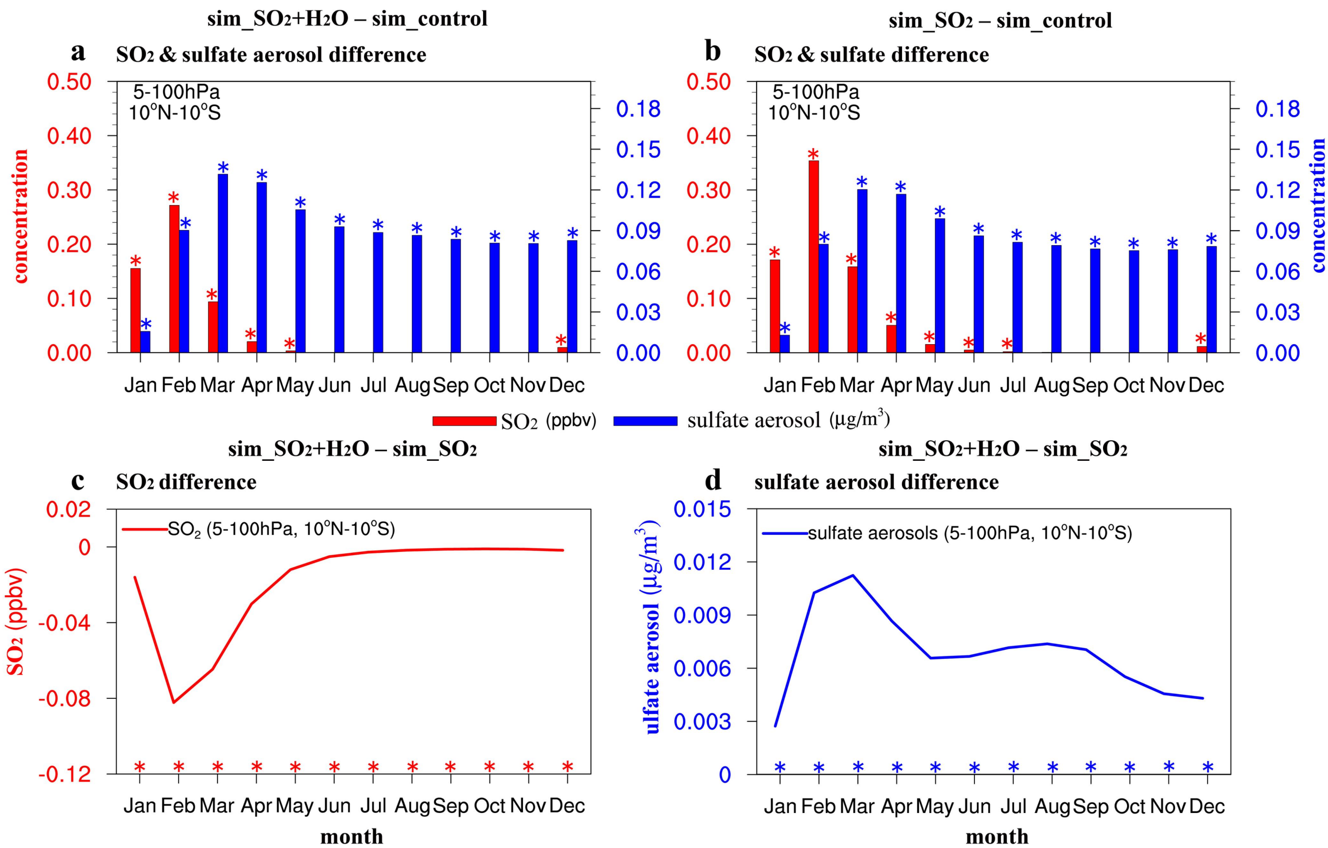

Figure 1. Simulated SO_2 and sulfate aerosols differences averaged over 5–100 hPa and 10°S–10°N (a) between sim_SO_2+H_2O and sim_control (sim_SO_2+H_2O – sim_control), (b) between sim_SO_2 and sim_control (sim_SO_2 – sim_control). (c) SO_2 difference, (d)

https://doi.org/10.5194/egusphere-2026-5104
Preprint. Discussion started: 23 September 2026

Sulfate aerosols difference between sim_SO_2+H_2O and sim_SO_2 (sim_SO_2+H_2O – sim_SO_2). Asterisks indicate that the difference is significant at the 95% confidence level. Here, the statistical significance is estimated by Student's t-statistic, which tests whether two sample populations have significantly different means (the same as follows).

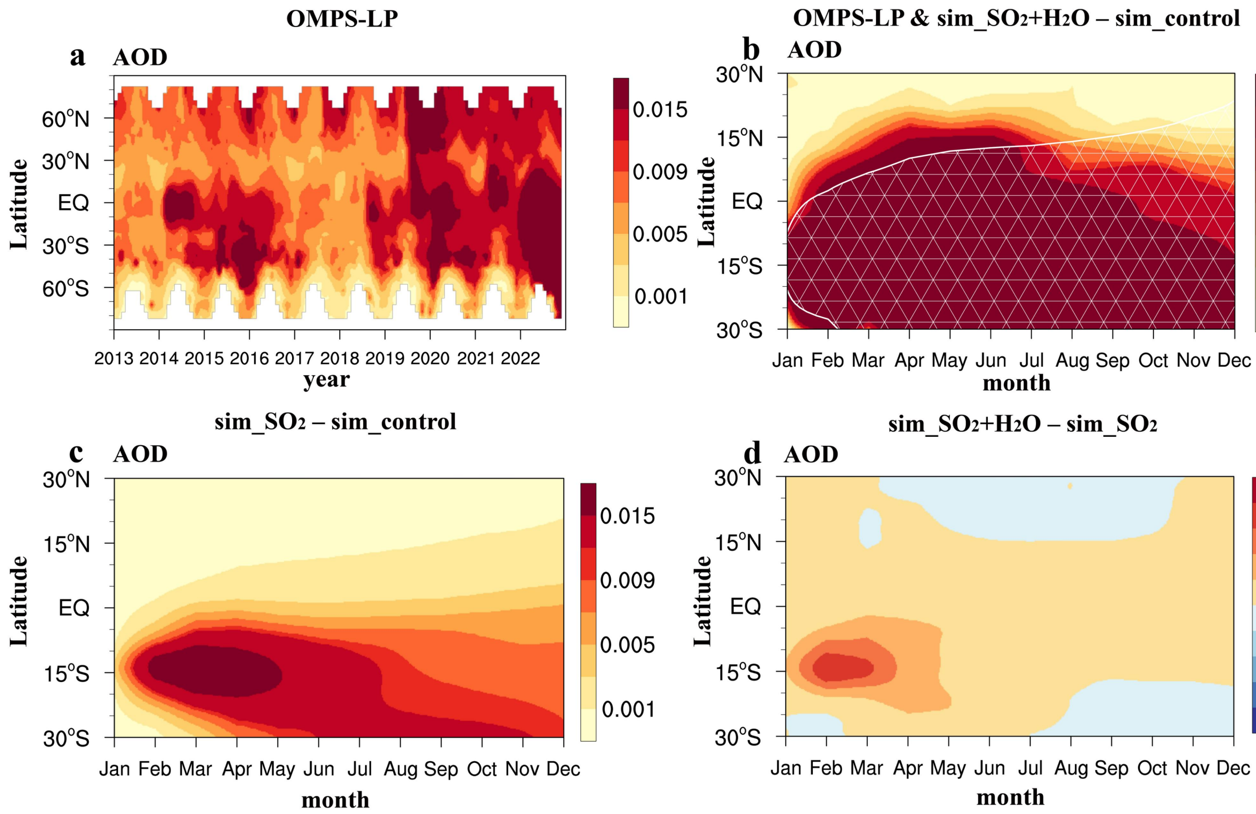

Figure 2. The stratospheric Zonal mean AOD distribution in the tropical stratosphere. (a) Zonal mean AOD_{510} in OMPS-LP L3 data for 2013–2022; (b) Zonal mean differences in OMPS-LP L3 data (2022 minus the average for 2020–2021), with the white grid showing zonal mean AOD at 550 nm (AOD_{550}) differences between sim_SO_2+H_2O and sim_control (sim_SO_2+H_2O – sim_control, only AOD values greater than 0.001 are plotted); (c) Zonal mean AOD_{550} differences between sim_SO_2 and sim_control (sim_SO_2 – sim_control,); (d) The Zonal mean AOD_{550} difference between sim_SO_2+H_2O and sim_SO_2 (sim_SO_2+H_2O – sim_SO_2).

Figure 2a shows the stratospheric AOD from OMPS-LP observations for 2013–2022. Elevated stratospheric AOD values appear in 2014–2016, followed by a gradual decline as aerosols are transported downward. Stratospheric AOD increases again in 2019 and becomes significantly larger in 2022 following the HTHH eruption (Fig. 2a). To isolate the eruption signal, stratospheric AOD anomalies in 2022 are calculated relative to the 2020–2021 mean. The observed stratospheric AOD anomalies indicate that stratospheric sulfate aerosols are transported poleward, particularly toward Antarctica via the BDC, while a portion remains in the tropical stratosphere (Fig. 2b). The spatial distribution of stratospheric AOD in sim_SO_2+H_2O experiment exhibits a similar pattern (Fig. 2b), whereas stratospheric AOD values in sim_SO_2 are weaker (Fig. 2c). The difference between the two simulations (sim_SO_2+H_2O minus sim_SO_2; Fig. 2d) further confirms that enhanced sulfate aerosol loading in sim_SO_2+H_2O is consistent with the accelerated sulfur conversion identified in Fig. 1.

https://doi.org/10.5194/egusphere-2026-5104
Preprint. Discussion started: 23 September 2026

3.2 QBO amplitude variation after HTHH eruption

Volcanic sulfate aerosols in the stratosphere can perturb the thermal structure and circulation of the tropical stratosphere, thereby modulate the QBO. Figure S4 shows the temporal evolution of the zonal mean zonal wind over 2°S–2°N at 5–100 hPa in the three experiments (sim_control, sim_SO_2, and sim_SO_2+H_2O). The timing of the QBO phase transition is similar across all experiments and consistent with the observed evolution in 2022 (Fig. S1), with a transition from westerly to easterly shear during the study period (Fig. S4). However, the magnitude and vertical propagation of zonal wind perturbations differ substantially among the experiments. In particular, zonal wind perturbations are significantly stronger in sim_SO_2+H_2O than in sim_SO_2 (Fig. S4b-c), indicating that the combined injection of H_2O and SO_2 primarily enhances the amplitude and downward propagation of the QBO, rather than altering the timing of its phase transition.

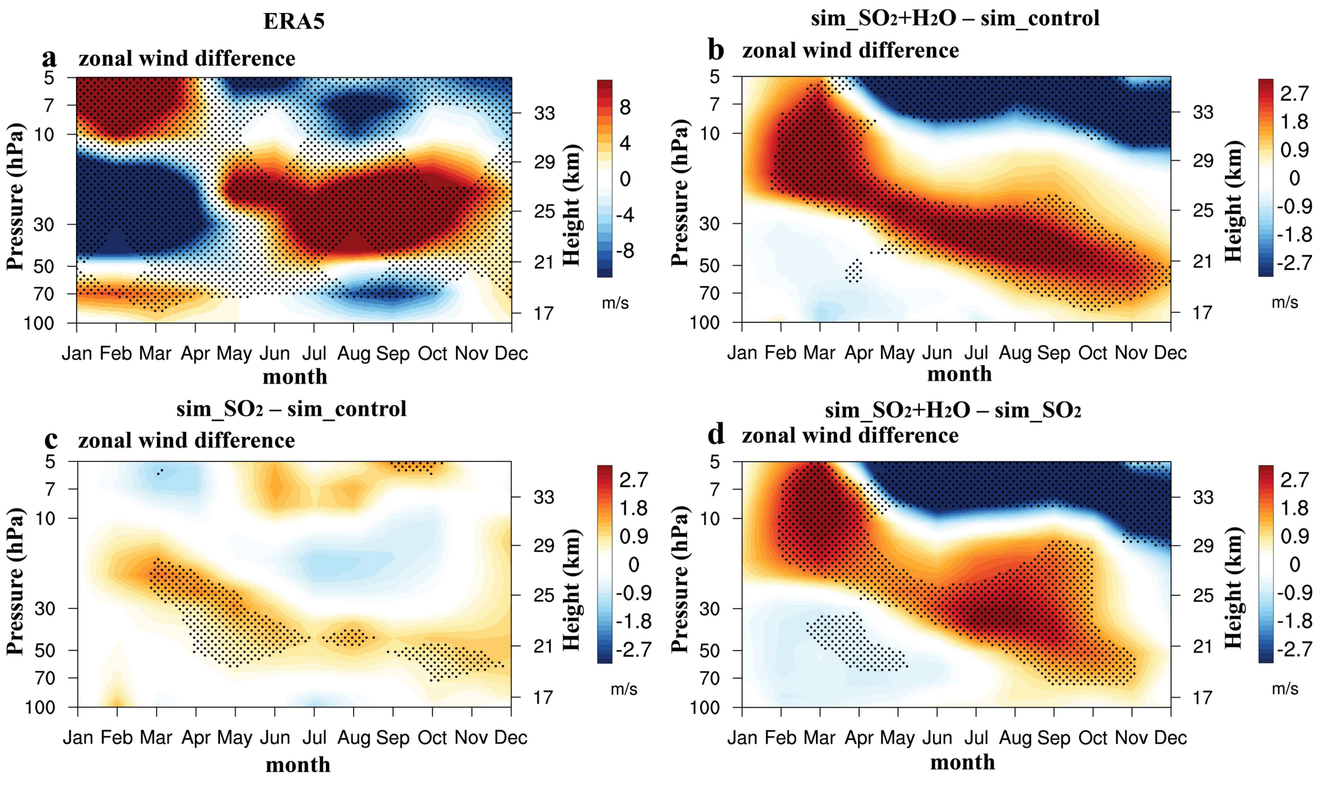

Figure 3. Zonal mean zonal wind differences in the tropical stratosphere (2°S–2°N) at 5–100 hPa. (a) Zonal mean zonal wind differences from ERA5 (2022 minus the climatology from 2007–2021), with anomalies removed the effects of the 2022 QBO (50 hPa) and ENSO using linear regression; (b) Zonal mean zonal wind anomalies between sim_SO_2+H_2O and sim_control (sim_SO_2+H_2O – sim_control); (c) same as (b), but between sim_SO_2 and sim_control (sim_SO_2 – sim_control); (d) same as (b), but between sim_SO_2+H_2O and sim_SO_2 (sim_SO_2+H_2O – sim_SO_2). Hatching indicates statistically significant areas at the 95% confidence level.

Figure 3a shows the zonal mean zonal wind anomalies over 2°S–2°N for 2022 derived from ERA5 (2022 minus the 2007–2021 climatology), which includes both natural variability in 2022 and the potential contribution from the HTHH eruption. To better isolate the volcanic signal, contributions from ENSO and the background QBO (50 hPa) are removed using linear regression. Following the HTHH eruption, positive zonal wind anomalies dominate the upper stratosphere (5–10 hPa) during January–March and descend to 10–50 hPa by April, continuing to propagate downward and persist throughout the year (Fig. 3a). In contrast, negative zonal wind anomalies appear at 10–50 hPa during January–March and at 5–20 hPa from April onward. In the lower stratosphere (50–100 hPa), significant positive zonal wind anomalies are evident from January to March, as well as in November and December (Fig. 3a).

To isolate the volcanic signal, Figure 3b presents the zonal wind perturbation relative to the control simulation (sim_SO_2+H_2O – sim_control). After the volcanic eruption, a clear positive zonal wind perturbation appears in the upper stratosphere (5–20 hPa) in January and gradually propagated downward, reaching approximately 100 hPa by September (Fig. 3b). Starting in April, a statistically significant positive zonal wind perturbation emerges near 30 hPa, exceeding 3 m s^{-1} and persisting until October (Fig. 3b). Meanwhile, a significant negative zonal wind perturbation appears at 5-20 hPa from April and continues through the end of the year. The major positive features are consistent between ERA5 and the model results, whereas some ERA5 anomalies (e.g., negative zonal wind anomalies at 10–50 hPa from January to March and at 50-100 hPa from August to October) are not reproduced in the sim_SO_2+H_2O experiment (Fig. 3 and b), suggesting that these features are more likely attributable to internal variability rather than the volcanic forcing, while positive zonal wind anomalies occur at 50–100 hPa from January to March. In comparison, the sim_SO_2 experiment also shows positive zonal wind perturbations relative to sim_control (sim_SO_2 – sim_control), but with weaker amplitude, lower onset altitude, and shorter duration (Fig. 3c). Although a statistically significant positive perturbation (95% confidence level) appears at 30 hPa from April, it persists only until early May (Fig. 3c). Moreover, no significant negative perturbation is simulated in the upper stratosphere (5–20 hPa), indicating that the negative wind response at these levels is primarily associated with H_2O injected by the HTHH eruption.

Although H_2O enhances sulfate formation by accelerating SO_2 oxidation, its direct contribution to sulfate mass remains relatively small (peaking at ~10% in February and March, Fig. 1). Therefore, the dynamical impact of H_2O is primarily reflected in the difference between sim_SO_2+H_2O and sim_SO_2. Figure 3d shows that zonal wind perturbations in sim_SO_2+H_2O are substantially stronger and exhibit more pronounced downward propagation than in sim_SO_2, with maximum differences exceeding 3 m s^{-1}. This indicates that H_2O injected by the HTHH eruption significantly enhances zonal wind perturbations and their downward propagation in the tropical stratosphere, thereby contributing to a stronger QBO response.

Figure S5 shows the QBO index at 30hPa in the three sets of experiments. All experiments (sim_control, sim_SO_2, and sim_SO_2+H_2O) reproduce the transition from EQBO to WQBO, consistent with Fig. S4. Compared to sim_control, the 30 hPa QBO index perturbations are weaker in sim_SO_2, while they are significantly stronger in sim_SO_2+H_2O (Fig. S5). Moreover, in sim_SO_2+H_2O, the QBO transitions more rapidly into the westerly phase. This behavior is consistent with the enhanced zonal wind perturbations shown in Fig. 3b, highlighting the significant modulation of the QBO by H_2O and SO_2 injected during the HTHH eruption.

https://doi.org/10.5194/egusphere-2026-5104
Preprint. Discussion started: 23 September 2026

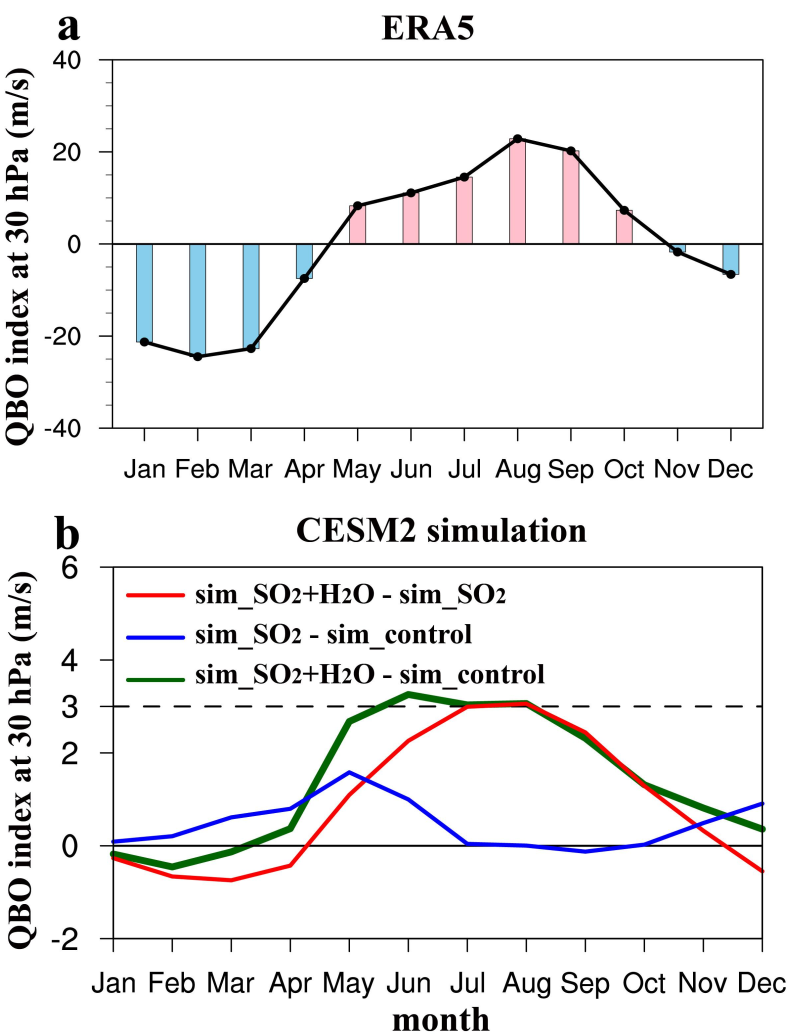

Figure 4. Monthly 30 hPa QBO index differences in the tropical stratosphere (2°S–2°N). (a) 30 hPa QBO index differences from ERA5 data (2022 minus the climatology from 2007–2021), with differences removed the effects of the 2022 QBO (50 hPa) and ENSO using linear regression; (b) 30 hPa QBO index differences between sim_SO_2+H_2O and sim_control (sim_SO_2+H_2O – sim_control, green line), 30 hPa QBO index differences between sim_SO_2 and sim_control (sim_SO_2 – sim_control, blue line), and the difference in 30 hPa QBO index between sim_SO_2+H_2O and sim_SO_2 (sim_SO_2+H_2O – sim_SO_2, red line).

Figure 4a shows the 30 hPa QBO index anomalies from ERA5 data (2022 relative to the 2007–2021 climatological mean). The index exhibits negative anomalies from January to April and then increases steadily, reaching a maximum in August before gradually declining thereafter. Positive anomalies persist from May to October before transitioning to negative anomalies in November and December. In sim_SO_2+H_2O, the 30 hPa QBO index perturbation strengthens relative to sim_control (sim_SO_2+H_2O – sim_control) from April onward and reaches maximum positive perturbations exceeding 3 m s^{-1} during June–August (Fig. 4b, green line). The positive perturbation then gradually weakens but remains positive and consistently higher than in sim_control for the remainder of the year. In contrast, the sim_SO_2 experiment produces weaker

https://doi.org/10.5194/egusphere-2026-5104
Preprint. Discussion started: 23 September 2026

perturbations (sim_SO_2 – sim_control, blue line), with smaller amplitudes and a less persistent positive phase compared to sim_SO_2+H_2O. A negative perturbation appears in September, and the positive perturbation remains weak from October to December. Although the maximum positive perturbation at 30 hPa in the sim_SO_2+H_2O experiment exceeds 3 m s^{-1}, it remains smaller than the corresponding anomaly in ERA5. This difference is expected, as volcanic forcing represents only one of several contributors to QBO variability. Moreover, the temporal evolution of the 30 hPa QBO index perturbations in sim_SO_2+H_2O closely follows the ERA5 anomalies, supporting a substantial volcanic contribution of SO_2 and H_2O injected by the HTHH eruption to the modulation of the stratospheric QBO.

Table 2. 30 hPa QBO index anomalies from May to October in 2022, based on CESM2 simulations and ERA5 data.

data	Category	May	June	July	August	September	October
ERA5	Anomaly	8.31 m/s	11.10 m/s	14.53 m/s	22.86 m/s	20.22 m/s	7.31 m/s
sim_SO_2	Anomaly	1.59 m/s	1.00 m/s	0.04 m/s	0.00 m/s	–0.13 m/s	0.02 m/s
	Percentage	19.13%	9.01%	0.28%	0.00%	–0.64%	0.27%
sim_SO_2+H_2O	Anomaly	2.68 m/s	3.26 m/s	3.03 m/s	3.06 m/s	2.31 m/s	1.31 m/s
	Percentage	32.25%	29.37%	20.85%	13.39%	11.42%	17.92%

We further quantify the 30 hPa QBO response to the HTHH eruption by comparing simulations with ERA5 for May-October 2022 (Table 2). In sim_SO_2, the volcanic-induced QBO index perturbation (sim_SO_2 – sim_control) is positive but much smaller, accounting for 9-19% of the ERA5 anomalies in May-June and less than 1% thereafter. In contrast, sim_SO_2+H_2O produces a substantially stronger volcanic-induced QBO index perturbation (sim_SO_2+H_2O – sim_control), accounting for approximately 11-32% of the ERA5 anomalies, with peaks in May-June (from 7 to 23 m s^{-1}). This comparison demonstrates that stratospheric H_2O injected by the HTHH eruption markedly amplifies the QBO response relative to the SO_2-only case, indicating a strong dynamical synergy between volcanic water vapor and sulfate aerosols.

Based on the evolution of the 30 hPa QBO response, April, July, and October are selected as representative stages. Figure 5 shows the zonal mean zonal wind perturbations in theses months. In April, sim_SO_2+H_2O (sim_SO_2+H_2O – sim_control) exhibits enhanced water vapor in the tropical middle and upper stratosphere, while sulfate aerosols are mainly confined to the middle and upper stratosphere in the Southern Hemisphere (Fig. 5a). Correspondingly, significant positive zonal wind perturbations relative to sim_control occur over 15°S–20°N at 7–50 hPa (95% confidence level). In sim_SO_2, positive zonal wind perturbations relative to sim_control are also found in the tropical regions influenced by sulfate aerosols, but their magnitude is substantially smaller than that in sim_SO_2+H_2O (Fig. 5a and b). The difference between sim_SO_2+H_2O and sim_SO_2 highlights this enhancement, with tropical positive wind perturbations exceeding those in sim_SO_2 by more than 3 m s^{-1} and beginning to propagate downward (Fig. 5c). By July, stratospheric water vapor in sim_SO_2+H_2O spreads further into the Northern Hemisphere, while sulfate aerosols descend toward the lower stratosphere (Fig. 5d). At the same time,

https://doi.org/10.5194/egusphere-2026-5104
Preprint. Discussion started: 23 September 2026

significantly positive zonal wind perturbations propagate downward to 30–50 hPa. Although a similar downward propagation is also simulated in sim_SO_2, the amplitude of the positive perturbations remains much smaller (Fig. 5e). The difference between the two experiments indicates that positive zonal wind perturbations in sim_SO_2+H_2O are about 3 m s^{-1} stronger than those in sim_SO_2, with a magnitude comparable to that in spring but occurring at lower altitudes (Fig. 5f). In October, positive zonal wind perturbations in sim_SO_2+H_2O continue to descend into the lower stratosphere (Fig. 5f). The zonal wind perturbations in sim_SO_2 are weaker, but also descend into the lower stratosphere, with positive differences located at slightly higher altitudes (Fig. 5h). The contrast between the two experiments remains pronounced, with substantially stronger positive perturbations in sim_SO_2+H_2O (Fig. 5i). These results indicate that water vapor injected by the HTHH eruption enhances the strength of zonal wind perturbations in the upper stratosphere and accelerates their downward propagation, thereby amplifying the dynamical response of the tropical stratosphere.

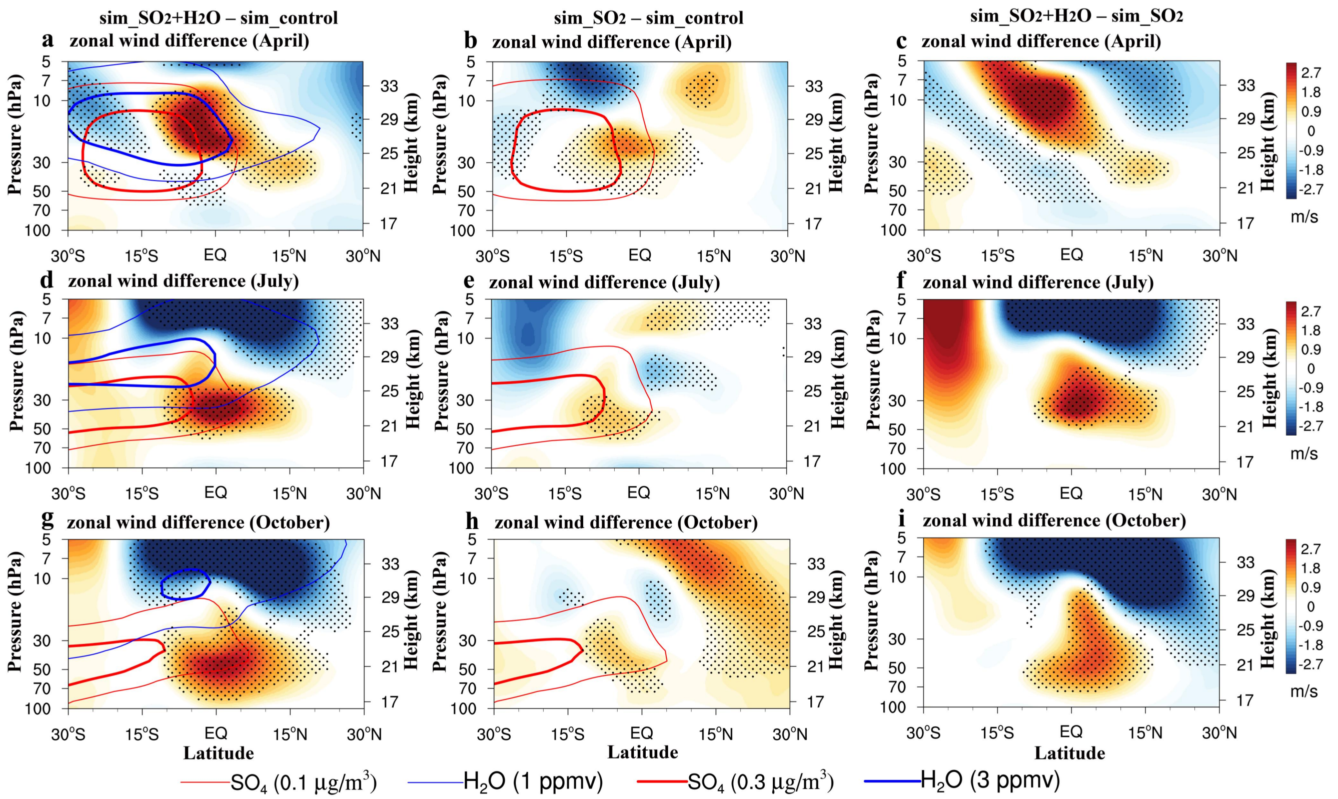

Figure 5. Zonal mean zonal wind anomalies in the tropical stratosphere. (a, d, g) Zonal mean zonal wind anomalies between sim_SO_2+H_2O and sim_control (sim_SO_2+H_2O – sim_control), with results for (a) April, (d) July, and (g) October, respectively, from top to bottom; (b, e, h) the same as (a, d, g), but showing the results between sim_SO_2 and sim_control (sim_SO_2 – sim_control); (c, f, i) the same as (a, d, g), but showing the results between sim_SO_2+H_2O and sim_SO_2 (sim_SO_2+H_2O – sim_SO_2). The thick red solid line represents sulfate aerosol concentration of 0.3 μg/m^3, and the thin solid line represents 0.1 μg/m^3; the thick blue solid line represents H_2O concentration of 3 ppmv, and the thin solid line represents 1 ppmv. Hatching indicates statistically significant areas at the 95% confidence level.

https://doi.org/10.5194/egusphere-2026-5104
Preprint. Discussion started: 23 September 2026

4 Dynamic mechanisms of QBO modification

The dynamic mechanisms through which volcanic eruptions modulate the QBO have been widely discussed in previous studies. For sulfate-dominated volcanic eruptions, lower-stratospheric warming induced by sulfate aerosols has been identified as an important driver of QBO modification (Aquila et al., 2014; Franke et al., 2021). Previous studies further suggest that the relative importance of the "upwelling mechanism" and the "thermal wind balance mechanism" varies across sulfate-dominated eruptions (Franke et al., 2021; Bittner et al., 2016). Sulfate aerosols absorb terrestrial longwave radiation and incoming near-infrared radiation, producing net warming in the lower tropical stratosphere (Babu et al., 2022; Timmreck, 2012; Toohey et al., 2011; Zuo et al., 2018). However, the HTHH eruption differs fundamentally from these cases because it injected a large amount of water vapor into the stratosphere, and the enhanced stratospheric H_2O leads to net radiative cooling rather than warming (Wang et al., 2023). Because the sign of the radiative forcing is reversed in the HTHH case, it is necessary to examine the stratospheric temperature response before analyzing how H_2O and sulfate aerosols influence the QBO through changes in tropical upwelling and thermal wind balance.

4.1 Stratospheric temperature variation after the HTHH eruption

In April, the spatial distribution of sulfate aerosols largely overlaps with that of H_2O in the sim_SO_2+H_2O experiment (sim_SO_2+H_2O – sim_control; Fig. 6a). Under these conditions, the radiative cooling induced by stratospheric H_2O dominates over the warming effects associated with sulfate aerosols, leading to a net temperature decrease in the upper stratosphere. The maximum negative temperature perturbation exceeds 1.0 K and is statistically significant at the 95% confidence level. In contrast, positive temperature perturbations are mainly confined to the lower stratosphere around 50 hPa, with a maximum of approximately 0.3 K, indicating that sulfate aerosol induced warming remains locally important at these levels. In the sim_SO_2 experiment (sim_SO_2 – sim_control; Fig. 6b), sulfate aerosols produce a pronounced temperature increase in the tropical upper stratosphere (5–20 hPa), with a maximum perturbation of about 0.9 K. This warming is associated with shortwave scattering by sulfate aerosols, which enhances upward radiative flux and leads to increased absorption above the aerosol layer. Although sulfate aerosols are also present below 20 hPa, enhanced scattering within the high-concentration regions reduces net radiative heating, resulting in weaker temperature increase at lower levels. The contribution of H_2O can be further isolated by comparing sim_SO_2+H_2O with sim_SO_2 (sim_SO_2+H_2O – sim_SO_2; Fig. 6c). Relative to the SO_2-only case, the presence of H_2O leads to a pronounced cooling in the middle and upper stratosphere, confirming that H_2O radiative effects dominate at these altitudes. Meanwhile, a weak but significantly warming (~0.2 K) persists near 50 hPa. This feature is consistent with previous CESM simulations showing that lower-stratospheric temperatures can respond directly to H_2O injected by the HTHH eruption, suggesting a contribution from the direct radiative effect of H_2O (Zhang et al., 2025). Thus, the weak warming near 50 hPa may partly reflect the direct radiative response to H_2O, although the sim_SO_2+H_2O – sim_SO_2 difference may also include indirect effects associated with H_2O-enhanced sulfate aerosol formation and dynamical adjustments.

https://doi.org/10.5194/egusphere-2026-5104
Preprint. Discussion started: 23 September 2026

The heating rate perturbations in April support this interpretation. In sim_SO_2+H_2O, the longwave heating rate shows a negative perturbation in the tropical Southern Hemisphere between 5 and 20 hPa (sim_SO_2+H_2O – sim_control; Fig. 7a), where H_2O perturbations are strongest, consistent with the upper-stratospheric cooling (Fig. 6a). In contrast, in the sim_SO_2 experiment, the shortwave heating rate exhibits a negative perturbation within the aerosol layer and a positive perturbation above it (sim_SO_2 – sim_control; Fig. 7b), reflecting the redistribution of radiative flux by sulfate aerosols.

In July, cooling associated with H_2O remains evident in the stratosphere, with a maximum perturbation of about 0.6 K in the sim_SO_2+H_2O experiment (sim_SO_2+H_2O – sim_control; Fig. 6d). Compared to April, both the spatial extent and magnitude of the cooling are reduced (Fig. 6a and d). Meanwhile, warming associated with sulfate aerosols is still present near 50 hPa, with a maximum of about 0.4 K. In the sim_SO_2 experiment, sulfate aerosols continue to produce strong warming in the tropical upper stratosphere (5–20 hPa), with maximum perturbations exceeding 0.9 K (sim_SO_2 – sim_control; Fig. 6e). Although H_2O still induces significant cooling in the upper stratosphere, the overall temperature decrease in the middle stratosphere is smaller than in April, partly due to the vertical redistribution of H_2O and the continued influence of sulfate aerosol warming. Near 50 hPa, a significant warming of about 0.4 K persists (Fig. 6e and f), consistent with the April pattern and likely related to the direct radiative effect of H_2O (Zhang et al., 2025). Correspondingly, heating rate perturbations in July show patterns similar to those in April. Regions of temperature perturbations in the tropical Southern Hemisphere closely correspond to longwave and shortwave heating rate perturbations (Fig. 7c and d), indicating that radiative processes continue to dominate the temperature response.

https://doi.org/10.5194/egusphere-2026-5104
Preprint. Discussion started: 23 September 2026

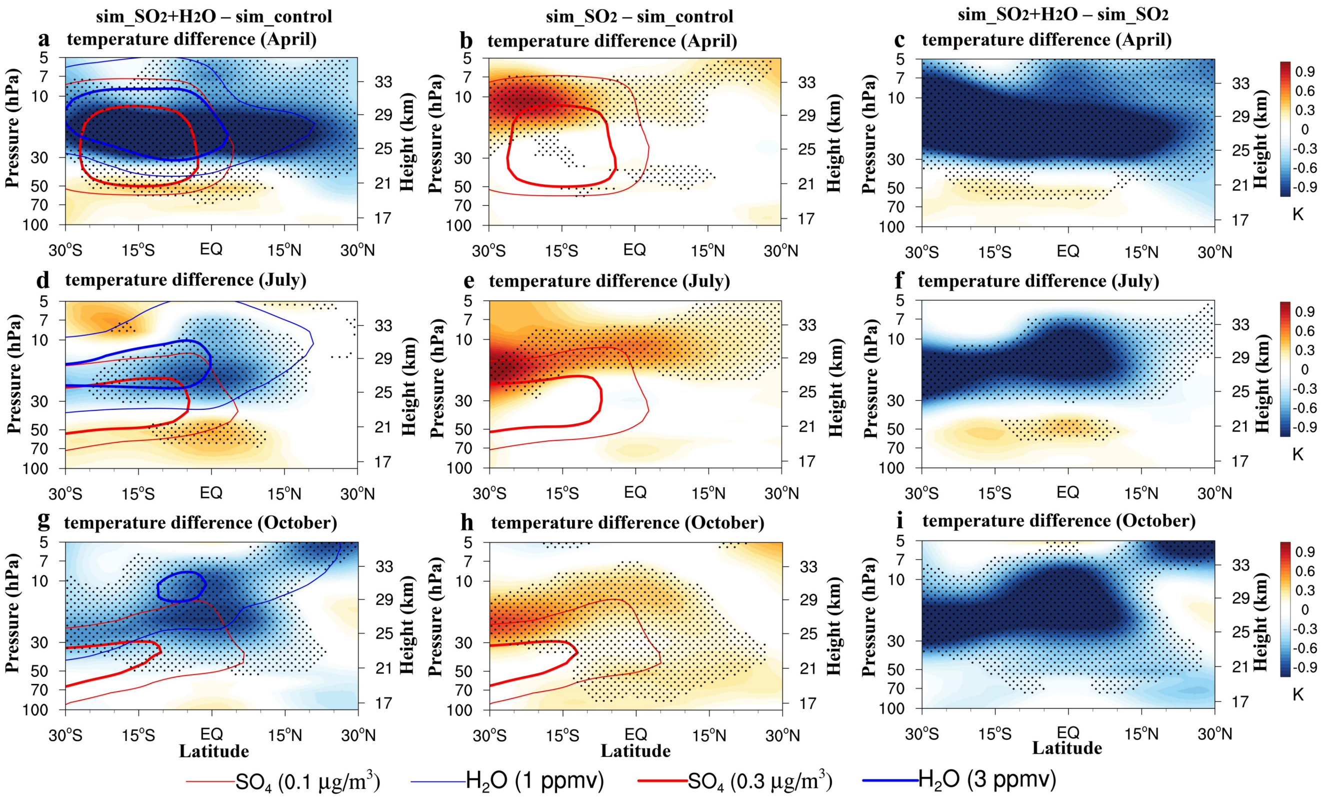

Figure 6. Same as Figure 5, but for zonal mean temperature differences.

In October, stratospheric H_2O is transported to higher altitudes, sustaining cooling in middle and upper stratosphere in sim_SO2+H2O relative to sim_control (sim_SO2+H2O – sim_control; Fig. 6g). In contrast, warming persists in the lower stratosphere, where sulfate aerosol perturbations remain important. In sim_SO_2, warming dominates the tropical stratosphere, particularly in the middle and lower stratosphere, reflecting the continued descent of sulfate aerosols (sim_SO_2 – sim_control; Fig. 6h). Relative to sim_SO_2, the cooling effect associated with H_2O remains strong in sim_SO_2+H_2O (Fig. 6i). The heating rate perturbations in October (Fig. 7e and f) exhibit spatial distributions that closely correspond to the temperature perturbations, indicating that the temperature response is primarily driven by radiative processes. Overall, these results indicate that H_2O injected by the HTHH eruption is the primary driver of stratospheric cooling, whereas sulfate aerosols induce comparatively weaker warming. The radiative effects of both components are concentrated mainly in the tropical Southern Hemisphere, while the longwave and shortwave heating rate perturbations in the tropical Northern Hemisphere remain relatively weak (Fig. 7).

https://doi.org/10.5194/egusphere-2026-5104
Preprint. Discussion started: 23 September 2026

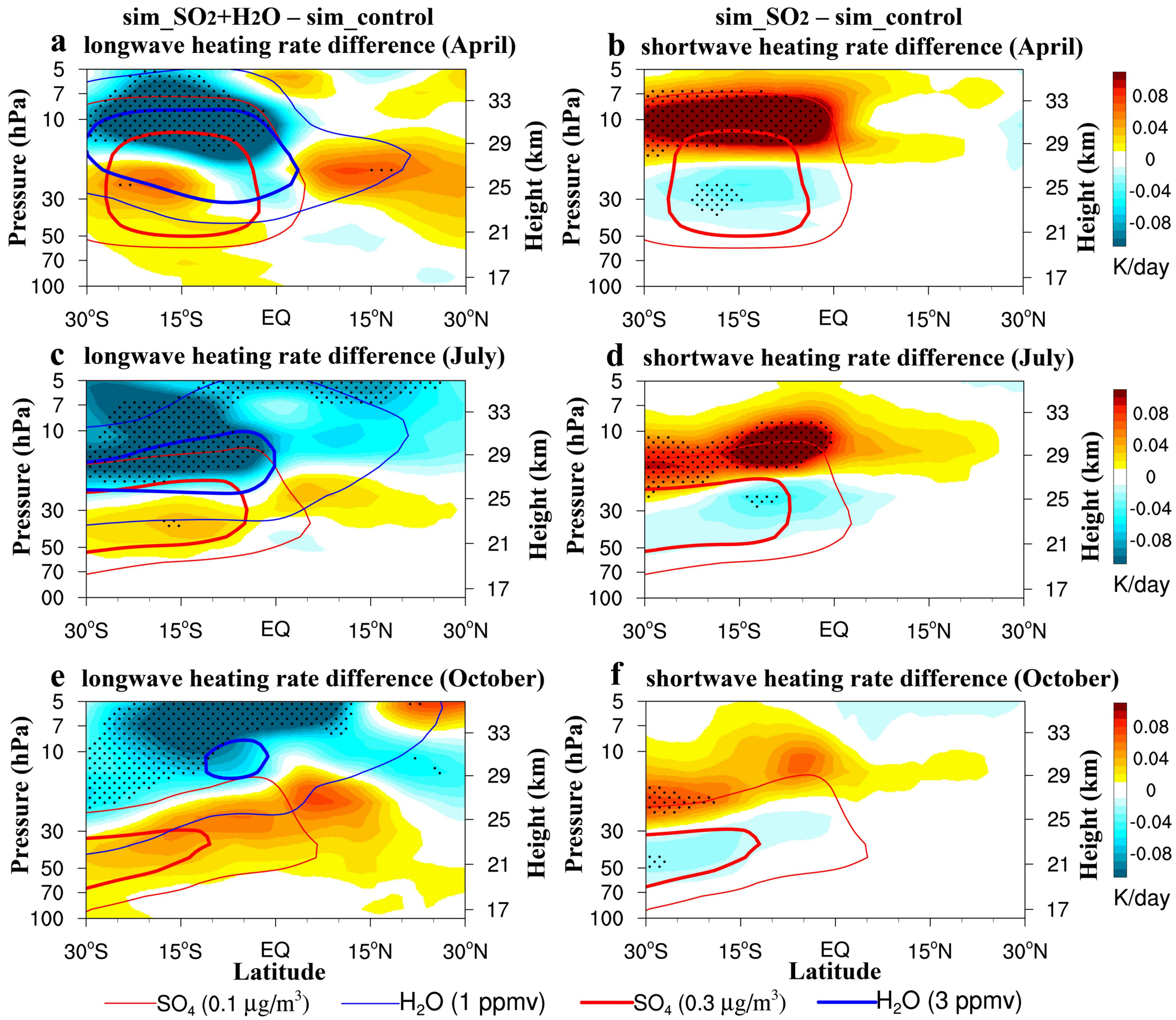

Figure 7. Zonal mean longwave heating rate and shortwave heating rate differences in the tropical stratosphere. (a, c, e) Zonal mean longwave heating rate differences between sim_SO₂+H₂O and sim_control (sim_SO₂+H₂O – sim_control), with results for (a) April, (d) July, and (g) October, respectively, from top to bottom; (b, d, f) the same as (a, c, e), but showing the zonal mean shortwave heating rate differences between sim_SO₂ and sim_control (sim_SO₂ – sim_control). The thick red solid line represents sulfate aerosol concentration of 0.3 μg/m³, and the thin solid line represents 0.1 μg/m³; the thick blue solid line represents H₂O concentration of 3 ppmv, and the thin solid line represents 1 ppmv. Hatching indicates statistically significant areas at the 95% confidence level.

Figure S6a further shows the zonal mean relationship between temperature and H_2O perturbations in sim_SO2+H2O relative to sim_control (sim_SO2+H2O – sim_control). In the upper stratosphere (10–30 hPa), temperature perturbations are strongly negatively correlated with H_2O perturbations ($R = -0.78$, 95% confidence level), providing robust statistical support for the

https://doi.org/10.5194/egusphere-2026-5104
Preprint. Discussion started: 23 September 2026

radiative cooling effect of H_2O identified above. By contrast, in sim_SO_2, temperature perturbations relative to sim_control (sim_SO_2 – sim_control) in the same region are positively correlated with sulfate aerosol perturbations (R = 0.65, 95% confidence level), consistent with the warming effect associated with sulfate aerosols.

Taken together, these results highlight pronounced hemispheric differences in the drivers of temperature variability. In the tropical Southern Hemisphere, temperature perturbations are strongly correlated with chemical perturbations (H_2O and sulfate aerosols), indicating that the thermal response is primarily controlled by volcanic radiative forcing. In the tropical Northern Hemisphere, the correlation is weaker, particularly between 15°N and 30°N. This suggests that temperature variability there is more strongly influenced by dynamical processes, such as changes in BDC and wave propagation, rather than by local radiative effects (Fig. 7 and S6). These findings further support the radiative modulation of stratospheric temperature by H_2O and SO_2 from the HTHH eruption in the Southern Hemisphere and their differential contributions to tropical zonal temperature anomalies during the transport process.

4.2 Modification of tropical upwelling

Enhanced tropical upwelling in the ascending branch of the BDC, driven by aerosol-induced warming, has been identified as an important mechanism for QBO modification in response to stratospheric aerosol perturbations (Aquila et al., 2014). Tropospheric planetary wave activity plays a major role in driving the BDC (Randel et al., 2002). Planetary wave propagation and wave-mean flow interaction in the stratosphere, diagnosed using the EP flux and its divergence provides, are therefore important for understanding how volcanic perturbations influence tropical upwelling and QBO variability (Andrews et al., 1987). However, residual upwelling is also constrained by the thermodynamic balance, because upward residual motion induces adiabatic cooling in the tropical stratosphere. Radiative heating or cooling perturbations can therefore modify the thermal constraint on the BDC and reshape the residual circulation response. In the HTHH case, the H_2O-induced radiative cooling discussed in Sect. 4.1 provides an additional thermal constraint that differs from the sulfate-aerosol warming mechanism in sulfate-dominated eruptions. Here, we examine how HTHH-induced perturbations in planetary waves 1 and 2, EP flux convergence, and radiative-dynamical coupling modify tropical upwelling and the downward propagation of QBO-related zonal wind perturbations.

In April, sim_SO_2+H_2O relative to sim_control (sim_SO_2+H_2O – sim_control) shows spatially heterogeneous changes in planetary waves 1 and 2 (Fig. S7a). Planetary wave 1 exhibits positive differences mainly in the Antarctic upper stratosphere, the tropical stratosphere between 30 and 100 hPa, and the Northern Hemisphere mid-to-high latitudes. Positive planetary wave 2 differences are primarily located over the Southern Hemisphere subtropics to mid-latitudes and the Northern Hemisphere mid-to-high latitudes. These wave perturbations are associated with negative EP flux divergence anomalies over the Antarctic, particularly over 70°S–90°S at 30–100 hPa and near 60°S at 5–20 hPa (Fig. 8a), indicating enhanced wave convergence and strengthened wave forcing on the mean flow in the Antarctic stratosphere. However, this high-latitude wave-forcing response does not directly explain the negative residual vertical velocity perturbations in the tropical Southern Hemisphere between 5 and 30 hPa (Fig. 9a), which indicate weakened local upwelling. Instead, the H_2O-driven radiative

https://doi.org/10.5194/egusphere-2026-5104
Preprint. Discussion started: 23 September 2026

cooling discussed in Sect. 4.1 modifies the upper-stratospheric thermal balance, reducing the requirement for adiabatic cooling by upwelling in this region and contributing to a weakening of the tropical upwelling branch of the BDC during this stage. The weakened upwelling reduces the upward advective tendency acting on zonal wind perturbations, allowing the positive upper stratospheric zonal wind perturbation to propagate downward more efficiently toward ~30 hPa (Fig. 5a). This H_2O-associated circulation adjustment, together with the pronounced temperature perturbations discussed in section 4.1, contributes to the enhanced 30 hPa QBO index response that becomes more evident after April (Fig. 4b). Meanwhile, planetary waves 1 and 2 are enhanced over the Northern Hemisphere mid-to-high latitudes (Fig. S7a). This enhanced wave activity suggests increased wave propagation into the stratosphere and is accompanied by localized EP flux convergence between 5 and 30 hPa (Fig. 8a), indicating strengthened wave forcing in this region. The enhanced convergence strengthens the Northern Hemisphere residual circulation and contributes to increased residual upwelling (Fig. 9a).

In the SO_2-only experiment, sim_SO_2 relative to sim_control (sim_SO_2 – sim_control) shows weaker and more regionally confined perturbations in planetary waves 1 and 2 than sim_SO_2+H_2O (Fig. S7b). Planetary wave 1 decreases in the Antarctic 5–30 hPa layer, whereas planetary wave 2 increases in the Southern Hemisphere mid-latitudes (Fig. S7b). Compared with sim_SO_2+H_2O, the absence of strong H_2O-induced radiative cooling makes the residual circulation response appear more directly linked to wave forcing. The enhanced Southern Hemisphere mid-latitude wave 2 propagates upward into the stratosphere and is associated with EP flux convergence (Fig. 8b), contributing to increased residual vertical velocity in the tropical Southern Hemisphere between 5 and 20 hPa and thus strengthened upwelling (Fig. 9b). However, this positive response does not extend downward continuously, as residual vertical velocity slightly decreases near the equator between 30 and 50 hPa (Fig. 9b). This vertically less coherent circulation response is consistent with the weaker downward propagation of positive zonal wind perturbations in sim_SO_2 than in sim_SO_2+H_2O (Fig. 5b and c). In the Northern Hemisphere, upward-propagating planetary waves 1 and 2 from high latitudes are reduced (Fig. S7b). Although EP flux convergence still occurs, it shifts downward into the mid-latitudes and is accompanied by enhanced divergence (Fig. 8b). This leads to decreased residual vertical velocity in the upper stratosphere (Fig. 9b), consistent with the positive temperature perturbations shown in Fig. 6b. Overall, SO_2-only forcing can still modulate stratospheric wave forcing and residual circulation, but the response remains less vertically coherent than in sim_ SO_2+H_2O. This contrast highlights the role of H_2O-induced radiative cooling in reshaping the thermal constraint on the BDC, and promoting stronger downward propagation of QBO-related zonal wind perturbations.

https://doi.org/10.5194/egusphere-2026-5104
Preprint. Discussion started: 23 September 2026

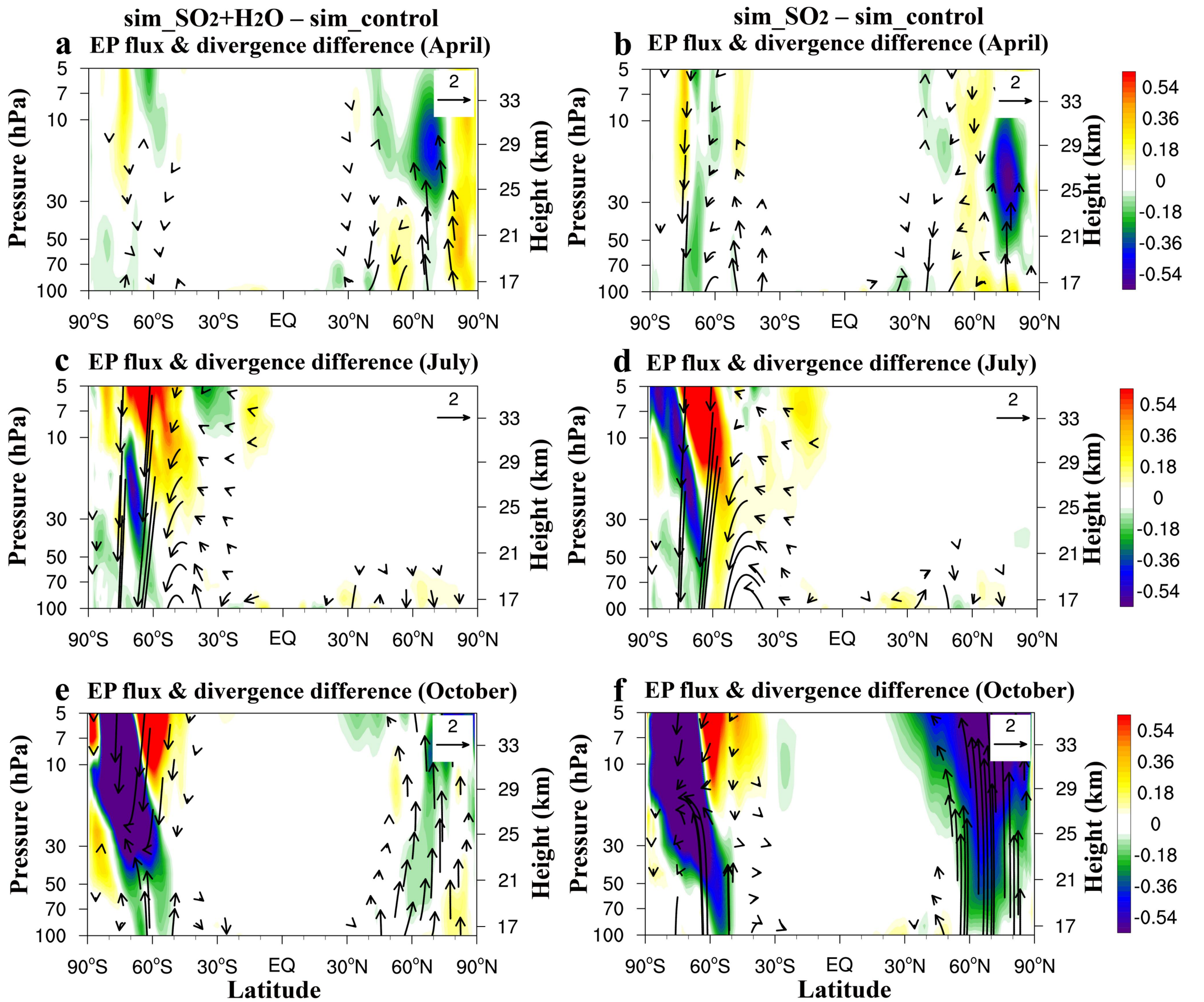

Figure 8. Zonal mean Eliassen-Palm (EP) flux and EP flux divergence differences in the stratosphere. (a, c, e) Zonal mean Eliassen-Palm (EP) flux and EP flux divergence between sim_SO$_2$+H$_2$O and sim_control (sim_SO$_2$+H$_2$O – sim_control), with results for (a) April, (d) July, and (g) October, respectively, from top to bottom; (b, d, f) the same as (a, c, e), but showing the results between sim_SO$_2$ and sim_control (sim_SO$_2$ – sim_control). The arrows (meridional and vertical components are divided by 10^6 and 10^5, respectively) represent the EP flux, and the shading indicates the EP flux divergence.

In July, sim_SO$_2$+H$_2$O relative to sim_control (sim_SO$_2$+H$_2$O – sim_control) shows enhanced planetary wave activity in the tropical stratosphere and mid-latitudes (Fig. S7c). Planetary wave 1 exhibits positive differences mainly in the tropical stratosphere, the Southern Hemisphere mid-latitudes between 30 and 100 hPa, and the Northern Hemisphere mid-latitudes between 5 and 30 hPa. Positive planetary wave 2 differences are evident from the subtropics to middle latitudes in both hemispheres, with extensions toward higher latitudes in the Southern Hemisphere. The associated EP flux indicates enhanced wave propagate toward the middle and high latitudes in Southern Hemisphere, with downward propagation and convergence near 60°S (Fig. 8c). However, strong EP flux divergence is also present in the 5–30 hPa layer, indicating weakened effective wave driving of the BDC at these levels. The residual vertical velocity response in July further indicates that the tropical upwelling response is not purely wave-driven. In sim_SO_2+H_2O, residual vertical velocity perturbations exhibit a meridionally structured response, with negative perturbations dominate on the Southern Hemisphere side of the tropics and localized positive perturbation near the equatorial upper stratosphere (Fig. 9c). This pattern indicates a redistribution of tropical upwelling rather than a uniform weakening. The H_2O-induced radiative cooling modifies the tropical thermal balance and contributes to this restructuring of the residual circulation. This restructured residual circulation is consistent with further downward propagation of positive zonal wind perturbations into the 30–50 hPa layer (Fig. 5d), thereby contributing to the enhanced 30 hPa QBO index response (Fig. 4b). The localized increase in equatorial residual vertical velocity is also consistent with the cooling between 5°S–15°N at 5–30 hPa (Fig. 6d), indicating continued coupling between radiative and dynamical processes.

In the SO_2-only experiment, sim_SO_2 relative to sim_control (sim_SO_2 – sim_control) exhibits vertical and latitudinal planetary wave perturbations distinct from that in sim_ SO_2+H_2O in July (Fig. S7d). Planetary wave 1 exhibits positive differences over most regions, except in the Antarctic 5–20 hPa layer, the Southern Hemisphere mid-to-high latitudes between 30 and 100 hPa, and the Northern Hemisphere mid-to-high latitudes between 5 and 20 hPa (Fig. S7d). Positive planetary wave 2 differences are mainly located in the Southern Hemisphere low-to-mid latitudes and the Northern Hemisphere mid-to-high latitudes. The associated EP flux patterns are broadly similar to those in sim_SO_2+H_2O, but the divergence-convergence structure is stronger and is accompanied by downward wave propagation over the Antarctic (Fig. 8d). This indicates stronger wave-driven forcing of the residual circulation in the SO_2-only case, contributing to increased residual vertical velocity on the Southern Hemisphere side of the tropics between 5 and 20 hPa and strengthened local upwelling (Fig. 9d). However, this positive perturbation is displaced south of the equator, while residual vertical velocity decreases near the equatorial 30 hPa region (Fig. 9d). This spatially offset circulation response is consistent with the weaker downward extension of positive zonal wind perturbation into the 30–50 hPa layer in sim_SO_2 than sim_SO_2+H_2O (Fig. 5d-e). In the tropical Northern Hemisphere, negative residual vertical velocity perturbation above 30 hPa are spatially consistent with the temperature increase shown in Fig. 6e, suggesting that dynamical adjustments may also contribute to the temperature response in the SO_2-only case.

https://doi.org/10.5194/egusphere-2026-5104
Preprint. Discussion started: 23 September 2026

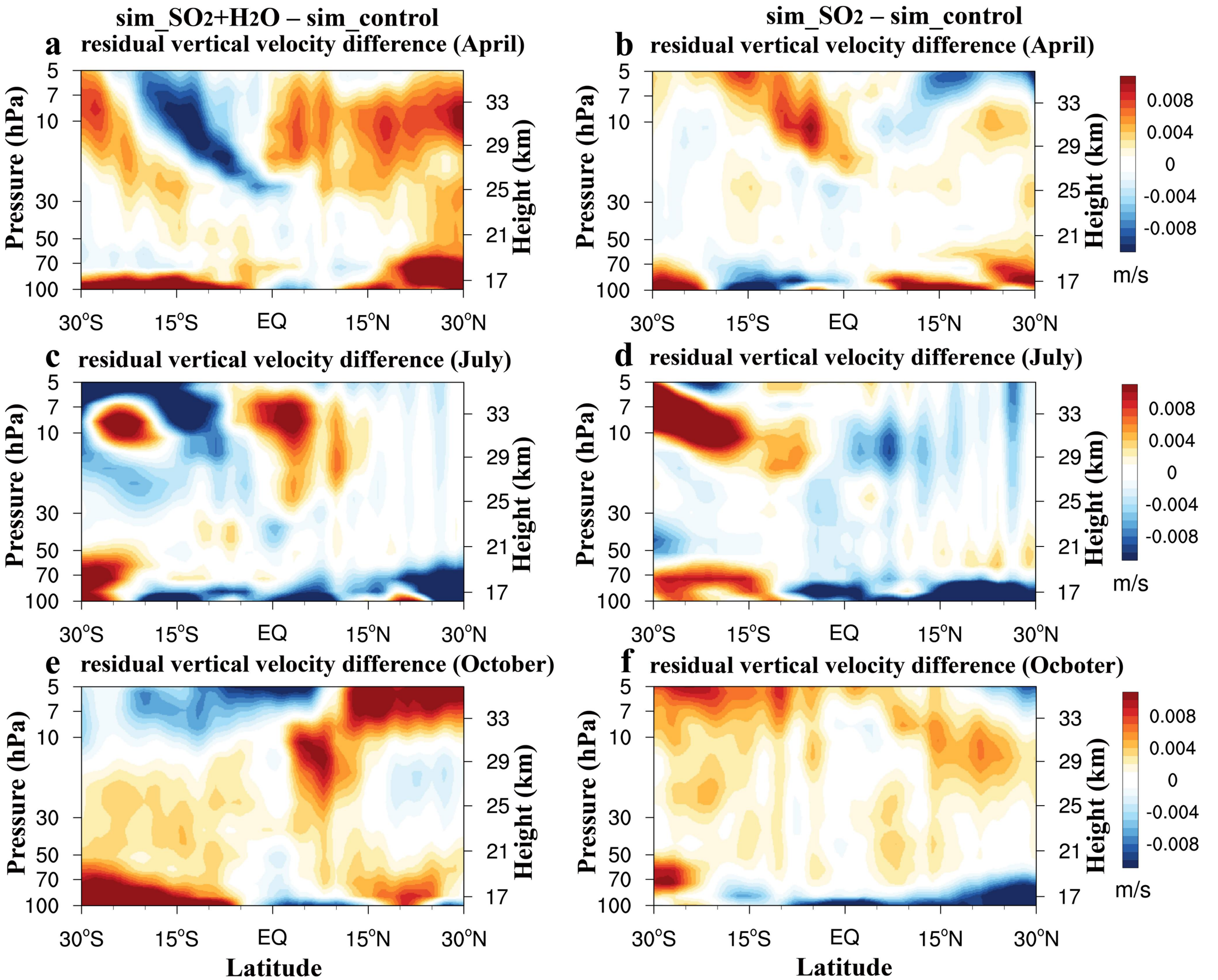

Figure 9. Zonal mean residual vertical velocity differences in the stratosphere. (a, c, e) Zonal mean residual vertical velocity difference between sim_SO_2+H_2O and sim_control (sim_SO_2+H_2O – sim_control), with results for (a) April, (d) July, and (g) October, respectively, from top to bottom; (b, d, f) the same as (a, c, e), but showing the results between sim_SO_2 and sim_control (sim_SO_2 – sim_control).

In October, both experiments exhibit circulation responses that differ from those in April and July. In sim_SO_2+H_2O relative to sim_control (sim_SO_2+H_2O – sim_control), planetary wave 1 shows positive differences mainly over the Southern Hemisphere mid-to-high latitudes, while positive planetary wave 2 differences are evident over the Antarctic and across15°S–30°N (Fig. S7e). The associated EP flux shows convergence over the Antarctic, accompanied by enhanced divergence near 60°S between 5 and 20 hPa (Fig. 8e), indicating active wave-mean flow interaction in the Southern Hemisphere high latitudes. These planetary-wave perturbations contribute to the October adjustment of the residual

https://doi.org/10.5194/egusphere-2026-5104
Preprint. Discussion started: 23 September 2026

circulation. Consistent with this wave-forcing response, residual vertical velocity perturbations are evident throughout the tropical stratosphere, indicating that the BDC structure is associated with decreased residual vertical velocity in the tropical Northern Hemisphere between 5 and 20 hPa and increased between 20–100 hPa (Fig. 9e), causing the positive zonal wind anomaly to propagate downward to the 50–100 hPa range (Fig. 5g). In sim_SO_2 (relative to sim_control; sim_SO_2 – sim_control), planetary wave 1 increases over the Antarctic 80°S–90°S range (Fig. S7f). Planetary wave 2 increases over the Antarctic 80°S–90°S and 40°S–10°N (Fig. S7f). Although the increase in planetary waves is limited over the Antarctic, the convergence process is strong (Fig. 8f). This leads to an increase in residual vertical velocity in the tropical Southern Hemisphere (Fig. 9f), while changes near the equator at 50–100 hPa remain small. Consequently, the positive zonal wind anomaly propagates downward only slightly (Fig. 5h).

It is worth noting that enhanced high-latitude wave activity and associated EP-flux convergence are evident in both experiments, although their spatial patterns differ between sim_SO_2+H_2O and sim_SO_2 (Figs. S7e-f and 8e-f). In im_SO_2+H_2O, positive residual vertical velocity perturbations are mainly confined to the tropical Northern Hemisphere near 5–20 hPa (Fig. 9e), whereas in sim_SO2 they extend more broadly across the tropical Northern Hemisphere between approximately 5 and 30 hPa (Fig. 9f). These contrasting upwelling structures are accompanied by different temperature responses in the tropical Northern Hemisphere (Figs. 6g–h), suggesting that the additional H_2O forcing further modulates the residual-circulation adjustment beyond the principal volcanic-forcing region.

In summary, H_2O and sulfate aerosols from the HTHH eruption modify planetary waves 1 and 2, alter EP flux convergence and divergence at different latitudes and altitudes, and thereby affect residual circulation and tropical upwelling. However, the comparison between sim_SO_2+H_2O and sim_SO_2 indicates that planetary wave forcing alone cannot fully explain the simulated residual circulation response. In particular, H_2O-induced radiative cooling modifies the thermal constraint on the tropical upwelling branch of the BDC, reshapes the residual circulation response, and reduces the upward advective tendency acting on zonal wind perturbations in key regions. This favours stronger downward propagation of positive zonal wind perturbations into the 30–100 hPa region and provides an important upwelling-related pathway through which the HTHH eruption modulated the amplitude and downward propagation of the stratospheric QBO.

4.3 Modification of thermal wind balance

Besides changes in tropical upwelling, QBO modification can also be influenced by changes in thermal wind balance (Aquila et al., 2014). As discussed in Sect. 4.1, the HTHH eruption induced substantial temperature perturbations in the tropical and subtropical stratosphere. These temperature perturbations modify the zonal-mean meridional temperature gradient ($\overline{T}_y$), and its meridional curvature ($\overline{T}_{yy}$), thereby affecting the vertical shear of the zonal-mean zonal wind through thermal wind balance. In April, sim_SO_2+H_2O relative to sim_control (sim_SO_2+H_2O – sim_control) shows pronounced negative temperature perturbations in the tropical middle and upper stratosphere (Fig. 6a), producing a spatially heterogeneous meridional temperature-gradient response. Positive $\overline{T}_y$ perturbations form a tilted band extending downward

https://doi.org/10.5194/egusphere-2026-5104
Preprint. Discussion started: 23 September 2026

and equatorward from around 30°S at 5–10 hPa toward the equatorial region near 30 hPa (Fig. 10a). These positive $\overline{T}_y$ perturbations correspond to significant negative $\overline{T}_{yy}$ perturbations (Fig. 11a), which are associated with enhanced westerly shear under thermal wind balance. This shear structure is consistent with the strong positive zonal wind perturbation mainly at 10–50 hPa in sim_SO_2+H_2O (Fig. 5a). Meanwhile, negative $\overline{T}_y$ perturbations are found in the tropical 5–10 hPa layer and in the subtropical regions of both hemispheres between 10 and 30 hPa (Fig. 10a), accompanied by corresponding positive $\overline{T}_{yy}$ perturbations (Fig. 11a). These structures favour easterly shear and are consistent with the negative zonal wind perturbations above the positive wind response (Fig. 5a), thereby shaping the vertical structure of the QBO-related wind perturbation during the early transition stage. Although the thermal-wind response is stronger in sim_SO_2+H_2O in April, its effect is mainly expressed as a vertically distributed shear structure over the 10–50 hPa layer and has not yet been fully projected onto the 30 hPa QBO index. This is consistent with the stronger 30 hPa QBO index response in sim_SO_2+H_2O emerging after April rather tha immediately in April (Fig. 4b).

In the SO_2-only experiment (sim_SO_2 – sim_control), a significant negative $\overline{T}_y$ perturbation appears in the tropical Southern Hemisphere between 5 and 20 hPa (Fig. 10b), accompanied by positive $\overline{T}_{yy}$ perturbations (Fig. 11b). This temperature-curavture structure favours easterly shear and is consistent with the negative zonal wind perturbation at 10–20 hPa (Fig. 5b). Compared with sim_SO_2+H_2O, sim_SO_2 shows weaker negative $\overline{T}_{yy}$ perturbations near 30 hPa (Fig. 11a-b), consistent with a weaker positive zonal wind perturbations near this level in April (Fig. 5a-b). The negative zonal wind perturbation aloft further indicates that the thermal-wind adjustment shapes the vertical shear structure of the QBO-related wind perturbation in the SO_2-only experiment. Therefore, the thermal wind balance mechanism contributes to the April positive zonal wind perturbation in both experiments, but the contribution is substantially stronger when H_2O is included. This contrast indicates that H_2O-induced temperature perturbation enhance the early thermal-wind adjustment, but the subsequent 30 hPa QBO index evolution cannot be attributed to thermal wind balance alone and reflects the combined effects of thermal wind balance and tropical upwelling changes. This result is consistent with previous studies showing that, during QBO phase transition, volcanic perturbations can induce westerly shear accompanied by easterly shear above it (Franke et al., 2021; Aquila et al., 2014).

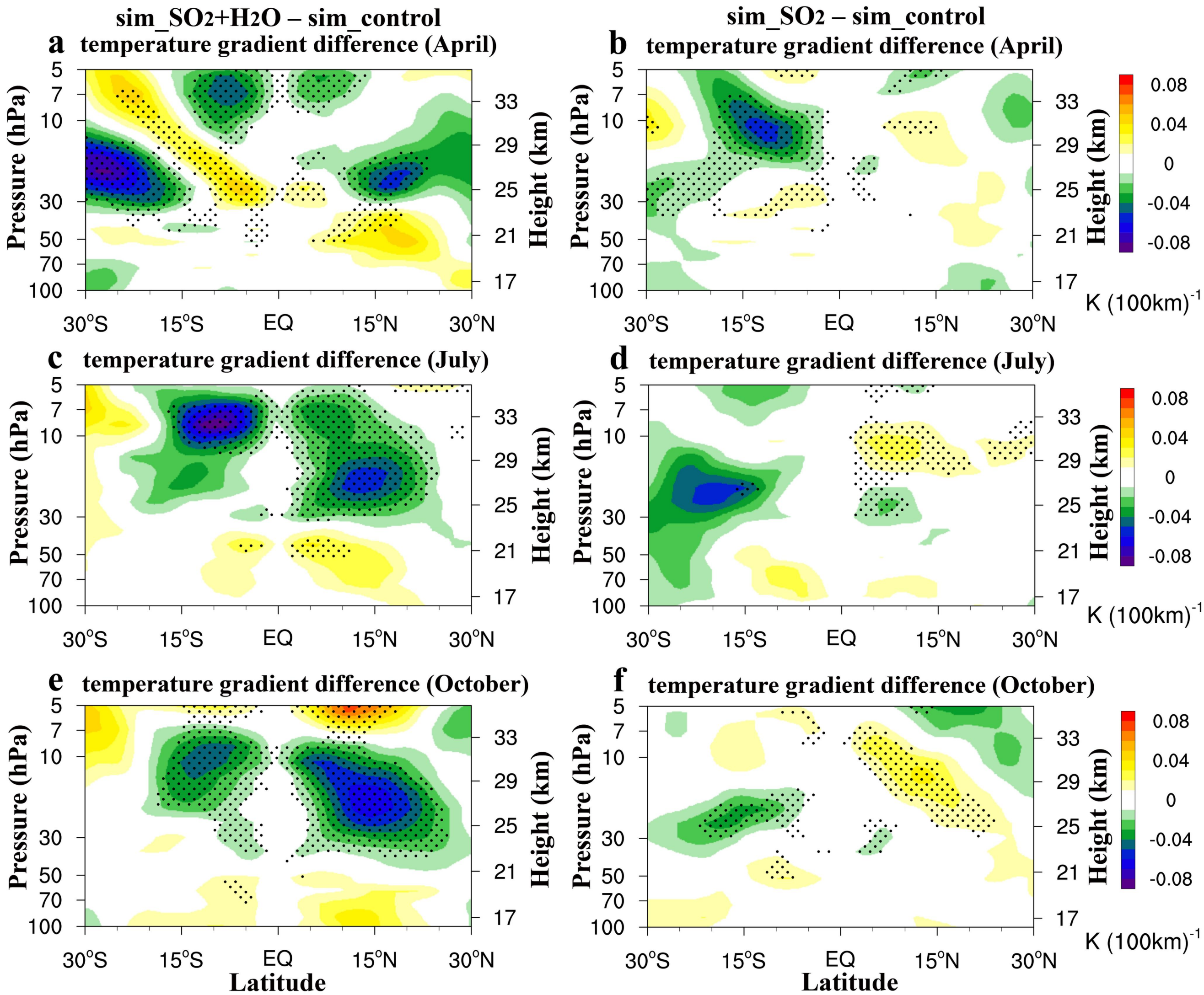

Figure 10. Zonal mean meridional temperature gradient ($\overline{T}_y$) differences in the stratosphere. (a, c, e) Zonal mean $\overline{T}_y$ difference between sim_SO₂+H₂O and sim_control (sim_SO₂+H₂O – sim_control), with results for (a) April, (d) July, and (g) October, respectively, from top to bottom; (b, d, f) the same as (a, c, e), but showing the results between sim_SO₂ and sim_control (sim_SO₂ – sim_control). Hatching indicates statistically significant areas at the 95% confidence level.

https://doi.org/10.5194/egusphere-2026-5104
Preprint. Discussion started: 23 September 2026

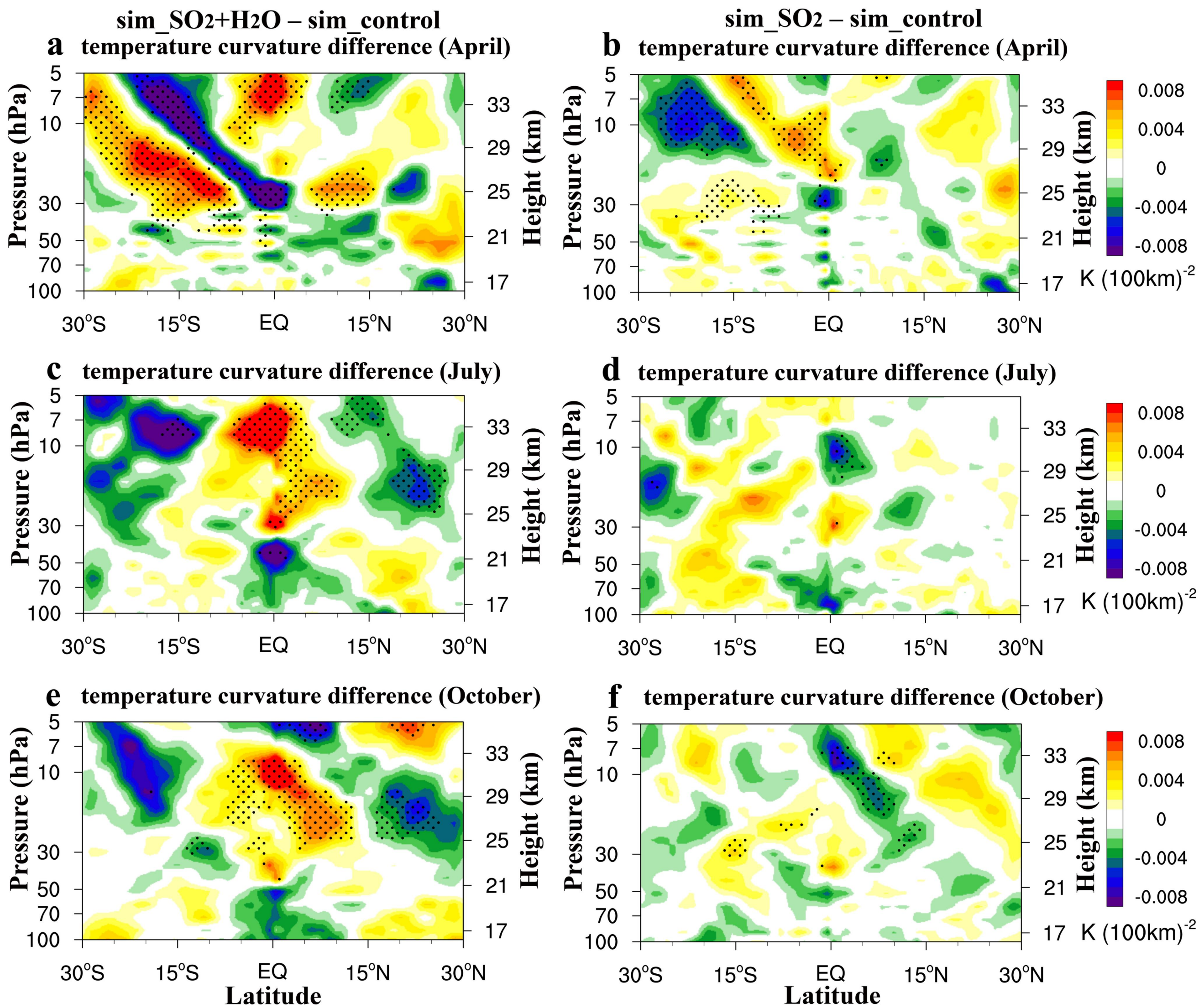

Figure 11. Same as in Figure 10, but for zonal mean meridional temperature curvature ($\overline{T}_{yy}$) differences.

In July, sim_SO₂+H₂O (sim_SO₂+H₂O – sim_control) shows significant positive $\overline{T}_y$ perturbations near 50 hPa (Fig. 10c), accompanied by negative $\overline{T}_{yy}$ perturbations (Fig. 11c). These structures are favorable for westerly shear, but their spatial extent is limited and they correspond only weakly to the positive zonal wind perturbation near 30–50 hPa (Fig. 5d). By contrast, significant negative $\overline{T}_y$ perturbations between 5 and 30 hPa (Fig. 10c), together with positive $\overline{T}_{yy}$ perturbations (Fig. 11c), are more clearly associated with the pronounced negative zonal wind perturbation above the positive wind response (Fig. 5d). In sim_SO₂ (sim_SO₂ – sim_control), no significant $\overline{T}_y$ or $\overline{T}_{yy}$ perturbations are found in the regions corresponding to the positive zonal wind perturbations (Fig. 10d and 11d), suggesting that thermal wind balance provides

https://doi.org/10.5194/egusphere-2026-5104
Preprint. Discussion started: 23 September 2026

only limited support for this perturbation in this experiment. The weak upper-level wind response in Fig. 5e further indicates that the thermal-wind contribution is small in the SO2-only experiment. Overall, the July results indicate that thermal wind balance is more clearly related to the upper-level wind-shear structure than to the positive zonal wind perturbation near 30–50 hPa. However, over 0°–20°N at 7–20 hPa, positive $\overline{\boldsymbol{T}}_{\boldsymbol{y}}$ perturbations and negative $\overline{\boldsymbol{T}}_{\boldsymbol{yy}}$ perturbations are present (Fig. 10d, 11d), which are consistent with local easterly wind-shear adjustment in this region (Fig. 5e).

In October, the thermal wind balance response in sim_SO_2+H_2O (sim_SO_2+H_2O – sim_control) is broadly similar to that in July (Fig. 10e and 11e). The $\overline{\boldsymbol{T}}_{\boldsymbol{y}}$ and $\overline{\boldsymbol{T}}_{\boldsymbol{yy}}$ perturbations make only a limited contribution to the positive zonal wind perturbations that have propagated downward into the 50–100 hPa layer (Fig. 5g, 10e, and 11e). Instead, regions with negative $\overline{\boldsymbol{T}}_{\boldsymbol{y}}$ and positive $\overline{\boldsymbol{T}}_{\boldsymbol{yy}}$ perturbations are more closely associated with negative zonal wind perturbations above the positive wind response. A similar behavior is found in sim_SO_2 (sim_SO_2 – sim_control; Fig. 5h, 10f, and 11f), where thermal wind balance contributes little to the weak positive zonal wind perturbation in the lower stratosphere but remains relevant for the negative zonal wind perturbations aloft.

The stratospheric temperature anomalies caused by H_2O and sulfur emissions from the HTHH eruption produced both positive $\overline{\boldsymbol{T}}_{\boldsymbol{y}}$ and negative $\overline{\boldsymbol{T}}_{\boldsymbol{yy}}$ anomalies in April. To maintain thermal wind balance, this temperature structure led to the formation of a westerly anomaly in the tropical stratosphere, thereby influencing the QBO. In the subsequent months of July and October, however, the contribution of this mechanism to the positive zonal wind anomaly gradually weakened, but it had a significant impact on the negative anomaly above the positive zonal wind anomaly. Furthermore, the contribution of the HTHH eruption to easterly anomalies was stronger in sim_SO_2+H_2O than in sim_SO_2 (Fig. 10–11). The stratospheric temperature exhibits more uniform meridional variation in sim_SO_2, leading to a weaker contribution to westerly anomalies, which is consistent with the findings of Franke et al., (2021).

In summary, the thermal wind balance mechanism contributes to the QBO response mainly during the early stage after the HTHH eruption. In April, H_2O and SO_2 injections produce zonal-mean meridional temperature-gradient and curvature perturbations that favor enhanced westerly shear in the tropical stratosphere, especially in sim_SO_2+H_2O. This contributes to the formation of positive zonal wind perturbations in the 10–50 hPa layer and shapes the vertical wind-shear structure during the early transition toward the WQBO phase. However, because this wind-shear response is vertically distributed and not yet fully projected onto 30 hPa in April, the stronger thermal-wind adjustment in sim_SO_2+H_2O does not immediately produce the largest 30 hPa QBO index response. Instead, the more pronounced 30 hPa response after April reflects the combined influence of the early thermal-wind adjustment and the upwelling-related downward propagation discussed in Sect. 4.2. In July and October, the contribution of thermal wind balance to the positive zonal wind perturbation weakens, while its influence on the negative zonal wind perturbation above the positive wind response remains evident. Compared with the SO_2-only experiment, sim_SO_2+H_2O shows stronger temperature-gradient and curvature perturbations, indicating that H_2O-induced temperature changes amplify the thermal wind adjustment and contribute to the vertical structure of the QBO-related zonal wind perturbations. Sulfate aerosols and H_2O from the HTHH eruption enhanced the westerly wind anomaly and

https://doi.org/10.5194/egusphere-2026-5104
Preprint. Discussion started: 23 September 2026

accelerated the downward propagation. Furthermore, for maintaining thermal-wind balance in the atmosphere, these aerosols and water vapor also induced a strong easterly wind anomaly above the westerly wind anomaly, thereby influencing stratospheric dynamic processes.

5 Conclusions

The HTHH eruption injected approximately 0.5 Tg of SO_2 and around 150 Tg of H_2O into the stratosphere on January 15 2022. Using MLS and OMPS-LP observations together with CESM-WACCM6 sensitivity simulations, this study investigated the effects of the water-rich HTHH eruption on the tropical QBO and the associated dynamic mechanisms. The results demonstrate that the large H_2O injection substantially modified the stratospheric response relative to the SO_2-only case. Enhanced stratospheric H_2O accelerated SO_2 oxidation through increased · OH production, leading to more rapid conversion of SO_2 to sulfate aerosols and enhanced sulfate aerosol loading in the tropical stratosphere. A portion of the injected H_2O and sulfate aerosols remained in the tropical stratosphere throughout 2022. However, their radiative effects differed substantially. H_2O-induced longwave cooling dominated the middle and upper tropical stratosphere, whereas sulfate aerosols contributed to localized warming in the lower stratosphere. As a result, the HTHH eruption produced a vertically structured temperature response that differs from the lower-stratospheric warming typically associated with sulfate-dominated volcanic eruptions.

The simulated QBO response was substantially stronger in sim_SO_2+H_2O than in sim_SO_2. In im_SO_2+H_2O, positive zonal wind perturbations developed in the upper stratosphere and subsequently extended downward to the 30-100 hPa layer. The corresponding 30 hPa QBO index perturbation exceeded 3 m s^{-1} during June–August and accounted for approximately 11–32% of the 2022 ERA5 30 hPa QBO index anomalies relative to the 2007–2021 climatology from May to October. In contrast, the SO_2-only experiment produced weaker and less persistent positive QBO index perturbations, accounting for less than 1% of the ERA5 anomalies after June. These results indicate that the injected H_2O was an important contributor to the enhanced QBO amplitude and downward extension of positive zonal wind perturbations.

The analysis of the upwelling mechanism indicates that planetary-wave and EP-flux perturbations provide the dynamical forcing for adjustments of the residual circulation, whereas H_2O-induced radiative cooling modifies the thermodynamic constraint on tropical upwelling. In April, the negative residual vertical velocity perturbations in the tropical Southern Hemisphere were more consistent with the additional H_2O-induced radiative cooling than with a simple wave-driven strengthening of the BDC. The associated reduction in local tropical upwelling weakened the upward advective tendency acting on positive zonal wind perturbations and favoured their initial downward extension. In July and October, the residual-circulation response became more vertically and meridionally heterogeneous. Compared with sim_SO_2, the additional H_2O forcing reshaped the tropical upwelling response to the already asymmetric volcanic perturbation, producing a more localized and hemispherically asymmetric residual-circulation structure. This circulation reorganization was associated with the stronger downward extension of positive zonal wind perturbations in sim_SO_2+H_2O.

The thermal wind balance mechanism also contributed to the QBO response, particularly during the early stage after the eruption. In April, the H_2O- and sulfate-induced temperature perturbations modified the meridional temperature gradient and its curvature, favouring a vertically structured combination of westerly shear at 10–50 hPa and easterly shear aloft. This thermal-wind response was stronger in sim_SO_2+H_2O and contributed to the early development of the positive zonal wind perturbation. This response differs from that expected for sulfate-dominated eruptions, in which lower-stratospheric sulfate warming more directly favours persistent westerly shear and can exert a stronger influence on the lower-stratospheric QBO evolution. In the HTHH case, H_2O-induced cooling in the middle and upper stratosphere produced a vertically contrasting thermal-wind response, which was most evident during the early stage and primarily shaped the vertical shear structure of the zonal wind perturbations. In July and October, thermal wind balance remained relevant to the upper-level negative zonal wind perturbations but contributed less directly to the positive zonal wind perturbations that had propagated into the lower stratosphere.

Overall, the HTHH eruption demonstrates that the QBO response to volcanic forcing cannot be understood solely in terms of sulfate-aerosol-induced lower-stratospheric warming. For water-rich eruptions, enhanced stratospheric H_2O can both alter sulfate aerosol evolution and impose substantial radiative cooling in the middle and upper stratosphere. The combined radiative and dynamical effects modify the thermal structure, residual circulation, and downward propagation of QBO-related zonal wind perturbations. These findings highlight the need to explicitly consider stratospheric H_2O, in addition to sulfur emissions, when assessing the dynamical impacts of future water-rich volcanic eruptions on the stratosphere.

Data availability

We are grateful to the National Aeronautics and Space Administration for making the aerosol profile product from OMPS-LP available at https://snpp-omps.gesdisc.eosdis.nasa.gov/data/SNPP_OMPS_Level3/OMPS_NPP_LP_L3_AER_MONTHLY.1/. The ERA5 reanalysis data can be obtained from https://cds.climate.copernicus.eu/datasets/reanalysis-era5-pressure-levels-monthly-means?tab=overview. The MLS satellite measurement is available at https://acdisc.gesdisc.eosdis.nasa.gov/data/Aura_MLS_Level3/. The WACCM6 dataset is archived on the Figshare platform at (Lu & Lou, 2025). All figures in this study are plotted by using NCAR Command Language (NCL), and related code can be found in NCL application examples (https://www.ncl.ucar.edu/Applications/).

Author contribution

SJ and JP participated in designing the simulations; JP performed the simulations and edited the code for analysis. Other co-authors participated in science discussions and suggested analyses. The paper was written by JP with contributions from all co-authors.

https://doi.org/10.5194/egusphere-2026-5104
Preprint. Discussion started: 23 September 2026

Competing interests

The contact author has declared that none of the authors has any competing interests.

Acknowledgements

We are grateful to the High-Performance Computing (HPC) at Nanjing University for doing the numerical calculations for this study on its Blade cluster system.

Financial support

This work was supported by the National Natural Science Foundation of China (42325506), Jiangsu Collaborative Innovation Centre for Climate Change of Nanjing University.

References

Andrews, D. G., Holton, J. R., and Leovy, C. B.: Middle atmosphere dynamics (p. 489), Academic press, 1987.

Anstey, J. A., Banyard, T. P., Butchart, N., Coy, L., Newman, P. A., Osprey, S., and Wright, C. J.: Prospect of Increased Disruption to the QBO in a Changing Climate, Geophys Res Lett, 48, e2021GL093058. https://doi.org/10.1029/2021GL093058, 2021.

Aquila, V., Garfinkel, C., Newman, P., Oman, L., and Waugh, D.: Modifications of the quasi-biennial oscillation by a geoengineering perturbation of the stratospheric aerosol layer, Geophys Res Lett, 41, 1738-1744, https://doi.org/10.1002/2013GL058818, 2014.

Babu, S. R., Nguyen, L. S. P., Sheu, G.-R., Griffith, S. M., Pani, S. K., Huang, H.-Y., and Lin, N.-H.: Long-range transport of La Soufrière volcanic plume to the western North Pacific: Influence on atmospheric mercury and aerosol properties, Atmos Environ, 268, 118806, https://doi.org/10.1016/j.atmosenv.2021.118806, 2022.

Baldwin, M. P., Gray, L. J., Dunkerton, T. J., Hamilton, K., Haynes, P. H., Randel, W. J., Holton, J. R., Alexander, M. J., Hirota, I., Horinouchi, T., Jones, D. B. A., Kinnersley, J. S., Marquardt, C., Sato, K., and Takahashi, M.: The quasi-biennial oscillation, Rev Geophys, 39, 179-229, https://doi.org/10.1029/1999RG000073, 2001.

Bittner, M., Timmreck, C., Schmidt, H., Toohey, M., and Krüger, K.: The impact of wave-mean flow interaction on the Northern Hemisphere polar vortex after tropical volcanic eruptions, J Geophys Res-Atmos, 121, 5281-5297, https://doi.org/10.1002/2015JD024603, 2016.

Bluth, G. J. S., Doiron, S. D., Schnetzler, C. C., Krueger, A. J., and Walter, L. S.: Global Tracking of the SO_2 Clouds from the June, 1991 Mount-Pinatubo Eruptions, Geophys Res Lett, 19, 151-154, https://doi.org/10.1029/91GL02792, 1992.

Bogenschutz, P. A., Gettelman, A., Hannay, C., Larson, V. E., Neale, R. B., Craig, C., and Chen, C. C.: The path to CAM6: coupled simulations with CAM5.4 and CAM5.5, Geosci Model Dev, 11, 235-255, https://doi.org/10.5194/gmd-11-235-2018, 2018.

Brenna, H., Kutterolf, S., Mills, M. J., Niemeier, U., Timmreck, C., and Krüger, K.: Decadal Disruption of the QBO by Tropical Volcanic Supereruptions, Geophys Res Lett, 48, https://doi.org/10.1029/2020GL089687, 2021.

Brown, F., Marshall, L., Haynes, P. H., Garcia, R. R., Birner, T., and Schmidt, A.: On the magnitude and sensitivity of the quasi-biennial oscillation response to a tropical volcaniceruption, Atmos Chem Phys, 23, 5335-5353, https://doi.org/10.5194/acp-23-5335-2023, 2023.

https://doi.org/10.5194/egusphere-2026-5104
Preprint. Discussion started: 23 September 2026

Carn, S. A., Krotkov, N. A., Fisher, B. L., and Li, C.: Out of the blue: Volcanic SO_2 emissions during the 2021-2022 eruptions of Hunga Tonga-Hunga Ha'apai (Tonga), Front Earth Sc-Switz, 10, https://doi.org/10.3389/feart.2022.976962, 2022.

DallaSanta, K., Orbe, C., Rind, D., Nazarenko, L., and Jonas, J.: Response of the Quasi-Biennial Oscillation to Historical Volcanic Eruptions, Geophys Res Lett, 48, https://doi.org/10.1029/2021GL095412, 2021.

Edmon, H. J., Hoskins, B. J., and Mcintyre, M. E.: Eliassen-Palm Cross-Sections for the Troposphere, J Atmos Sci, 37, 2600-2616, https://doi.org/10.1175/1520-0469(1980)037<2600:EPCSFT>2.0.CO;2, 1980.

Ern, M., Hoffmann, L., Rhode, S., and Preusse, P.: The Mesoscale Gravity Wave Response to the 2022 Tonga Volcanic Eruption: AIRS and MLS Satellite Observations and Source Backtracing, Geophys Res Lett, 49, https://doi.org/10.1029/2022GL098626, 2022.

Ferraro, A. J., Highwood, E. J., and Charlton-Perez, A. J.: Stratospheric heating by potential geoengineering aerosols, Geophys Res Lett, 39, https://doi.org/10.1029/2011GL049761, 2012.

Franke, H. and Giorgetta, M. A.: Toward the Direct Simulation of the Quasi-Biennial Oscillation in a Global Storm-Resolving Model, J Adv Model Earth Sy, 16, https://doi.org/10.1029/2024MS004381, 2024.

Franke, H., Niemeier, U., and Visioni, D.: Differences in the quasi-biennial oscillation response to stratospheric aerosol modification depending on injection strategy and species, Atmos Chem Phys, 21, 8615-8635, https://doi.org/10.5194/acp-21-8615-2021, 2021.

Fu, Q., Wang, M. C., White, R. H., Pahlavan, H. A., Alexander, B., and Wallace, J. M.: Quasi-Biennial Oscillation and Sudden Stratospheric Warmings during the Last Glacial Maximum, Atmosphere, 11, https://doi.org/10.3390/atmos11090943, 2020.

Gao, C. Y., Naik, V., Horowitz, L. W., Ginoux, P., Paulot, F., Dunne, J., Mills, M., Aquila, V., and Colarco, P.: Volcanic Drivers of Stratospheric Sulfur in GFDL ESM4, J Adv Model Earth Sy, 15, https://doi.org/10.1029/2022MS003532, 2023.

Garfinkel, C. I. and Hartmann, D. L.: The Influence of the Quasi-Biennial Oscillation on the Troposphere in Winter in a Hierarchy of Models. Part II: Perpetual Winter WACCM Runs, J Atmos Sci, 68, 2026-2041, https://doi.org/10.1175/2011JAS3702.1, 2011.

Ge, W. D., Liu, J. F., Yi, K., Xu, J. Y., Zhang, Y. Z., Hu, X. R., Ma, J. M., Wang, X. J., Wan, Y., Hu, J. Y., Zhang, Z. B., Wang, X. L., and Tao, S.: Influence of atmospheric in-cloud aqueous-phase chemistry on the global simulation of SO_2 in CESM2, Atmos Chem Phys, 21, 16093-16120, https://doi.org/10.5194/acp-21-16093-2021, 2021.

Gettelman, A., Mills, M., Kinnison, D., Garcia, R., Smith, A., Marsh, D., Tilmes, S., Vitt, F., Bardeen, C., and McInerny, J.: The whole atmosphere community climate model version 6 (WACCM6), J Geophys Res-Atmos, 124, 12380-12403, https://doi.org/10.1029/2019JD030943, 2019.

Guarino, M. V., Gardner, C. S., Feng, W. H., Funke, B., García-Comas, M., López-Puertas, M., Kupilas, M. M., Marsh, D. R., and Plane, J. M. C.: A Novel Gravity Wave Transport Parametrization for Global Chemistry Climate Models: Description and Validation, J Adv Model Earth Sy, 16, https://doi.org/10.1029/2023MS003938, 2024.

Hersbach, H., Bell, B., Berrisford, P., Hirahara, S., Horányi, A., Muñoz-Sabater, J., Nicolas, J., Peubey, C., Radu, R., Schepers, D., Simmons, A., Soci, C., Abdalla, S., Abellan, X., Balsamo, G., Bechtold, P., Biavati, G., Bidlot, J., Bonavita, M., De Chiara, G., Dahlgren, P., Dee, D., Diamantakis, M., Dragani, R., Flemming, J., Forbes, R., Fuentes, M., Geer, A., Haimberger, L., Healy, S., Hogan, R. J., Hólm, E., Janisková, M., Keeley, S., Laloyaux, P., Lopez, P., Lupu, C., Radnoti, G., de Rosnay, P., Rozum, I., Vamborg, F., Villaume, S., and Thépaut, J. N.: The ERA5 global reanalysis, Q J Roy Meteor Soc, 146, 1999-2049, https://doi.org/10.1002/qj.3803, 2020.

Holton, J.: An Introduction to Dynamic Meteorology, 4th Edition, Academic Press, Oxford, U. K, 2004.

Jaross, G., Bhartia, P. K., Chen, G., Kowitt, M., Haken, M., Chen, Z., Xu, P., Warner, J., and Kelly, T.: OMPS Limb Profiler instrument performance assessment, J Geophys Res-Atmos, 119, 4399-4412, https://doi.org/10.1002/2013jd020482, 2014.

Kremser, S., Thomason, L. W., von Hobe, M., Hermann, M., Deshler, T., Timmreck, C., Toohey, M., Stenke, A., Schwarz, J. P., and Weigel, R.: Stratospheric aerosol—Observations, processes, and impact on climate, Rev. Geophys, 54, 278-335, https://doi.org/10.1002/2015RG000511, 2016.

Labitzke, K.: Stratospheric Temperature-Changes after the Pinatubo Eruption, J Atmos Terr Phys, 56, 1027-1034, https://doi.org/10.1016/0021-9169(94)90039-6, 1994.

Liu, X., Ma, P. L., Wang, H., Tilmes, S., Singh, B., Easter, R. C., Ghan, S. J., and Rasch, P. J.: Description and evaluation of a new four-mode version of the Modal Aerosol Module (MAM4) within version 5.3 of the Community Atmosphere Model, Geosci Model Dev, 9, 505-522, https://doi.org/10.5194/gmd-9-505-2016, 2016.

Liu, Y. M., Dong, X. Y., Wang, M. H., Emmons, L. K., Liu, Y. W., Liang, Y., Li, X., and Shrivastava, M.: Analysis of secondary organic aerosol simulation bias in the Community Earth System Model (CESM2.1), Atmos Chem Phys, 21, 8003-8021, 10.5194/acp-21-8003-2021, https://doi.org/10.5194/acp-21-8003-2021, 2021.

Lu, J. P., & Lou, S. J.: Simulation data the CESM2 model [Dataset]. figshare. https://doi.org/10.6084/m9.figshare.28802405.v1, 2025.

Lu, J. P., Xie, F., Tian, W. S., Li, J. P., Feng, W. H., Chipperfield, M., Zhang, J. K., and Ma, X.: Interannual Variations in Lower Stratospheric Ozone During the Period 1984-2016, J Geophys Res-Atmos, 124, 8225-8241, https://doi.org/10.1029/2019JD030396, 2019.

Lu, J. P., Lou, S. J., Huang, X., Xue, L., Ding, K., Liu, T. Y., Ma, Y., Wang, W. K., and Ding, A. J.: Stratospheric Aerosol and Ozone Responses to the Hunga Tonga-Hunga Ha'apai Volcanic Eruption, Geophys Res Lett, 50, e2022GL102315, https://doi.org/10.1029/2022gl102315, 2023.

Mills, M. J., Schmidt, A., Easter, R., Solomon, S., Kinnison, D. E., Ghan, S. J., Neely III, R. R., Marsh, D. R., Conley, A., and Bardeen, C. G.: Global volcanic aerosol properties derived from emissions, 1990–2014, using CESM1 (WACCM), Journal of Geophysical Research: Atmospheres, 121, 2332-2348, https://doi.org/10.1002/2015JD024290, 2016.

Mo, R. Z. and Hu, D. Z.: Modulation of QBO on the relationship between stratospheric polar vortex and surface air temperature over Eurasia during early winter, Clim Dynam, 62, 7819-7838, https://doi.org/10.1007/s00382-024-07308-w, 2024.

Niemeier, U., Richter, J. H., and Tilmes, S.: Differing responses of the quasi-biennial oscillation to artificial SO_2 injections in two global models, Atmos Chem Phys, 20, 8975-8987, https://doi.org/10.5194/acp-20-8975-2020, 2020.

Proud, S. R., Prata, A. T., and Schmauss, S.: The January 2022 eruption of Hunga Tonga-Hunga Ha'apai volcano reached the mesosphere, Science, 378, 554-557, https://doi.org/10.1126/science.abo4076, 2022.

Quaglia, I., Timmreck, C., Niemeier, U., Visioni, D., Pitari, G., Brodowsky, C., Brühl, C., Dhomse, S. S., Franke, H., Laakso, A., Mann, G. W., Rozanov, E., and Sukhodolov, T.: Interactive stratospheric aerosol models' response to different amounts and altitudes of SO_2 injection during the 1991 Pinatubo eruption, Atmos Chem Phys, 23, 921-948, https://doi.org/10.5194/acp-23-921-2023, 2023.

Randel, W. J. and Wu, F.: Isolation of the ozone QBO in SAGE II data by singular-value decomposition, J Atmos Sci, 53, 2546-2559, https://doi.org/10.1175/1520-0469(1996)053<2546:IOTOQI>2.0.CO;2, 1996.

Randel, W. J., Wu, F., and Stolarski, R.: Changes in column ozone correlated with the stratospheric EP flux, J Meteorol Soc Jpn, 80, 849-862, https://doi.org/10.2151/jmsj.80.849, 2002.

Randel, W. J., Johnston, B. R., Braun, J. J., Sokolovskiy, S., Vömel, H., Podglajen, A., and Legras, B.: Stratospheric Water Vapor from the Hunga Tonga-Hunga Ha'apai Volcanic Eruption Deduced from COSMIC-2 Radio Occultation, Remote Sens, 15, https://doi.org/10.3390/rs15082167, 2023.

Richter, J. H., Tilmes, S., Mills, M. J., Tribbia, J. J., Kravitz, B., MacMartin, D. G., Vitt, F., and Lamarque, J. F.: Stratospheric dynamical response and ozone feedbacks in the presence of SO_2 injections, J Geophys Res-Atmos, 122, 12,557-12,573, https://doi.org/10.1002/2017JD026912, 2017.

Santer, B. D., Solomon, S., Bonfils, C., Zelinka, M. D., Painter, J. F., Beltran, F., Fyfe, J. C., Johannesson, G., Mears, C., Ridley, D. A., Vernier, J. P., and Wentz, F. J.: Observed multivariable signals of late 20th and early 21st century volcanic activity, Geophys Res Lett, 42, 500-509, https://doi.org/10.1002/2014gl062366, 2015.

Scaife, A. A., Athanassiadou, M., Andrews, M., Arribas, A., Baldwin, M., Dunstone, N., Knight, J., MacLachlan, C., Manzini, E., Müller, W. A., Pohlmann, H., Smith, D., Stockdale, T., and Williams, A.: Predictability of the quasi-biennial oscillation and its northern winter teleconnection on seasonal to decadal timescales, Geophys Res Lett, 41, 1752-1758, https://doi.org/10.1002/2013GL059160, 2014.

Schoeberl, M. R., Wang, Y., Ueyama, R., Taha, G., Jensen, E., and Yu, W.: Analysis and Impact of the Hunga Tonga-Hunga Ha'apai Stratospheric Water Vapor Plume, Geophys Res Lett, 49, e2022GL10024810, https://doi.org/10.1029/2022GL100248, 2022.

Sellitto, P., Podglajen, A., Belhadji, R., Boichu, M., Carboni, E., Cuesta, J., Duchamp, C., Kloss, C., Siddans, R., Bègue, N., Blarel, L., Jegou, F., Khaykin, S., Renard, J. B., and Legras, B.: The unexpected radiative impact of the Hunga Tonga eruption of 15th January 2022, Commun Earth Environ, 3, 288, https://doi.org/10.1038/s43247-022-00618-z, 2022.

Solomon, S., Kinnison, D., Bandoro, J., and Garcia, R.: Simulation of polar ozone depletion: An update, J Geophys Res-Atmos, 120, 7958-7974, https://doi.org/10.1002/2015jd023365, 2015.

Son, S. W., Lim, Y., Yoo, C. H., Hendon, H. H., and Kim, J.: Stratospheric Control of the Madden-Julian Oscillation, J Clim, 30, 1909-1922, https://doi.org/10.1175/JCLI-D-16-0620.1, 2017.

Stone, K. A., Solomon, S., and Kinnison, D. E.: On the Identification of Ozone Recovery, Geophys Res Lett, 45, 5158-5165, https://doi.org/10.1029/2018GL077955, 2018.

Stone, K. A., Solomon, S., Kinnison, D. E., Pitts, M. C., Poole, L. R., Mills, M. J., Schmidt, A., Neely III, R. R., Ivy, D., and Schwartz, M. J.: Observing the impact of Calbuco volcanic aerosols on South Polar ozone depletion in 2015, Journal of Geophysical Research: Atmospheres, 122, 11,862811,879, https://doi.org/10.1002/2017JD026987, 2017.

Tilmes, S., Richter, J. H., Mills, M. J., Kravitz, B., MacMartin, D. G., Vitt, F., Tribbia, J. J., and Lamarque, J. F.: Sensitivity of aerosol distribution and climate response to stratospheric SO2 injection locations, J Geophys Res-Atmos, 122, 12,591-12,615, https://doi.org/10.1002/2017JD026888, 2017.

Tilmes, S., Hodzic, A., Emmons, L., Mills, M., Gettelman, A., Kinnison, D. E., Park, M., Lamarque, J. F., Vitt, F., and Shrivastava, M.: Climate forcing and trends of organic aerosols in the Community Earth System Model (CESM2), J Adv Model Earth Syst, 11, 4323-4351, https://doi.org/10.1029/2019MS001827, 2019.

Timmreck, C.: Modeling the climatic effects of large explosive volcanic eruptions, WIREs Clim Change, 3, 545-564, https://doi.org/10.1002/wcc.192, 2012.

Toohey, M. and Sigl, M.: Volcanic stratospheric sulfur injections and aerosol optical depth from 500 BCE to 1900 CE, Earth Syst Sci Data, 9, 809-831, https://doi.org/10.5194/essd-9-809-2017, 2017.

Toohey, M., Krüger, K., Niemeier, U., and Timmreck, C.: The influence of eruption season on the global aerosol evolution and radiative impact of tropical volcanic eruptions, Atmos Chem Phys, 11, 12351-12367, https://doi.org/10.5194/acp-11-12351-2011, 2011.

Trepte, C. R. and Hitchman, M. H.: Tropical Stratospheric Circulation Deduced from Satellite Aerosol Data, Nature, 355, 626-628, https://doi.org/10.1038/355626a0, 1992.

Wang, F., Arseneault, D., Boucher, E., Gennaretti, F., Yu, S. L., and Zhang, T. W.: Tropical volcanoes synchronize eastern Canada with Northern Hemisphere millennial temperature variability, Nat Commun, 13, https://doi.org/10.1038/s41467-022-32682-6, 2022.

Wang, X. Y., Randel, W., Zhu, Y. Q., Tilmes, S., Starr, J., Yu, W. D., Garcia, R., Toon, O. B., Park, M., Kinnison, D., Zhang, J., Bourassa, A., Rieger, L., Warnock, T., and Li, J. H. Y.: Stratospheric Climate Anomalies and Ozone Loss Caused by the Hunga Tonga-Hunga Ha'apai Volcanic Eruption, J Geophys Res-Atmos, 128, e2023JD03948010 , https://doi.org/10.1029/2023JD039480, 2023.

Wang, Z., Zhang, J., Zhao, S., and Li, D.: The joint effect of mid-latitude winds and the westerly quasi-biennial oscillation phase on the Antarctic stratospheric polar vortex and ozone, Atmos. Chem. Phys., 25, 3465-3480, https://doi.org/10.5194/acp-25-3465-2025, 2025.

Waters, J. W., Froidevaux, L., Harwood, R. S., Jarnot, R. F., Pickett, H. M., Read, W. G., Siegel, P. H., Cofield, R. E., Filipiak, M. J., Flower, D. A., Holden, J. R., Lau, G. K. K., Livesey, N. J., Manney, G. L., Pumphrey, H. C., Santee, M. L., Wu, D. L., Cuddy, D. T., Lay, R. R., Loo, M. S., Perun, V. S., Schwartz, M. J., Stek, P. C., Thurstans, R. P., Boyles, M. A., Chandra, K. M., Chavez, M. C., Chen, G. S., Chudasama, B. V., Dodge, R., Fuller, R. A., Girard, M. A., Jiang, J. H., Jiang, Y. B., Knosp, B. W., LaBelle, R. C., Lam, J. C., Lee, K. A., Miller, D., Oswald, J. E., Patel, N. C., Pukala, D. M., Quintero, O., Scaff, D. M., Van Snyder, W., Tope, M. C., Wagner, P. A., and Walch, M. J.: The Earth Observing System Microwave Limb Sounder (EOS MLS) on the Aura satellite, Ieee T Geosci Remote, 44, 1075-1092, https://doi.org/10.1109/tgrs.2006.873771, 2006.

Xia, Y., Wang, Y. W., Huang, Y., Hu, Y. Y., Bian, J. C., Zhao, C. F., and Sun, C.: Significant Contribution of Stratospheric Water Vapor to the Poleward Expansion of the Hadley Circulation in Autumn Under Greenhouse Warming, Geophys Res Lett, 48, e2021GL094008, https://doi.org/10.1029/2021GL094008, 2021.

https://doi.org/10.5194/egusphere-2026-5104
Preprint. Discussion started: 23 September 2026

Xia, Y., Li, X., Hu, Y. Y., Huang, Y., Zhao, C. F., Xie, F., Guo, J. Q., Lan, J. W. J., Lin, Q. F., and Yuan, S. A.: Significant Contribution of Paleogeography to Stratospheric Water Vapor Variations in the Past 250 Million Years, Geophys Res Lett, 49, 10.1029/2022gl100919, https://doi.org/10.1029/2022GL100919, 2022.

Zhang, J. K., Xie, F., Ma, Z. C., Zhang, C. Y., Xu, M., Wang, T., and Zhang, R. H.: Seasonal Evolution of the Quasi-biennial Oscillation Impact on the Northern Hemisphere Polar Vortex in Winter, J Geophys Res-Atmos, 124, 12568-12586, https://doi.org/10.1029/2019jd030966, 2019.

Zhang, T. S., Xie, F., Xia, Y., Wang, Y. W., Zhou, L. Y., Xiang, X. Y., and Niu, Y. L.: Impact of middle stratospheric water vapor increase on polar vortices: a case study of the Tonga volcanic eruption, Theor Appl Climatol, 156, https://doi.org/10.1007/s00704-024-05276-z, 2025.

Zhou, X., Mann, G. W., Feng, W. H., Dhomse, S. S., and Chipperfield, M. P.: The Influence of Internal Climate Variability on Stratospheric Water Vapor Increases After Large-Magnitude Explosive Tropical Volcanic Eruptions, Geophys Res Lett, 50, e2023GL103076, https://doi.org/10.1029/2023GL103076, 2023.

Zhou, X., Dhomse, S. S., Feng, W. H., Mann, G., Heddell, S., Pumphrey, H., Kerridge, B. J., Latter, B., Siddans, R., Ventress, L., Querel, R., Smale, P., Asher, E., Hall, E. G., Bekki, S., and Chipperfield, M. P.: Antarctic Vortex Dehydration in 2023 as a Substantial Removal Pathway for Hunga Tonga-Hunga Ha'apai Water Vapor, Geophys Res Lett, 51, e2023GL107630, https://doi.org/10.1029/2023GL107630, 2024.

Zuo, M., Man, W. M., Zhou, T. J., and Guo, Z.: Different Impacts of Northern, Tropical, and Southern Volcanic Eruptions on the Tropical Pacific SST in the Last Millennium, J Clim, 31, 6729-6744, https://doi.org/10.1175/Jcli-D-17-0571.1, 2018.